Theses and Dissertations--Mechanical Engineering

Mechanical Engineering

PRESSURE-DRIVEN STABILIZATION OF CAPACITIVE DEIONIZATION

Landon S. Caudill
University of Kentucky, lsc5624@gmail.com
Digital Object Identifier: https://doi.org/10.13023/ETD.2018.122

PRESSURE-DRIVEN STABILIZATION
OF CAPACITIVE DEIONIZATION

_____

THESIS

_____

A thesis submitted in partial fulfillment of the requirements
for the degree of Master of Science in Mechanical Engineering
in the College of Engineering at the University of Kentucky

By

Landon Scott Caudill

Lexington, Kentucky

Director: Dr. Kunlei Liu, Professor of Mechanical Engineering

Lexington, Kentucky

2018

ABSTRACT OF THESIS

PRESSURE-DRIVEN STABILIZATION
OF CAPACITIVE DEIONIZATION

The effects of system pressure on the performance stability of flow-through capacitive deionization (CDI) cells was investigated. Initial data showed that the highly porous carbon electrodes possessed air/oxygen in the micropores, and the increased system pressure boosts the gases solubility in saline solution and carries them out of the cell in the effluent. Upon applying a potential difference to the electrodes, capacitive-based ion adsorption occurs in competition with faradaic reactions that consume oxygen. Through the addition of backpressure, the rate of degradation decreases, allowing the cell to maintain its salt adsorption capacity (SAC) longer. The removal of oxygen from the pore space of the electrodes makes it no longer immediately accessible to faradaic reactions, thus hindering the rate of reactions and giving the competing ion adsorption an advantage that is progressively seen throughout the life of the cell. A quick calculation shows that the energy penalty to power the pump is fairly insignificant, especially in comparison to the cost of replacing the electrodes in the cell. Thus, operating at elevated pressures is shown to be cost effective for continuous operation through the reduced electrode replenishment costs.

KEYWORDS: Capacitive deionization, Pressure-Driven Oxygen Dissolution, Henry's Law, Salt Adsorption Rate, Salt Adsorption Capacity

Landon Scott Caudill

April 9, 2018

PRESSURE-DRIVEN STABILIZATION
OF CAPACITIVE DEIONIZATION

By

Landon Scott Caudill

Dr. Kunlei Liu
(Director of Thesis)

Dr. Haluk Karaca
(Director of Graduate Studies)

April 9, 2018

ACKNOWLEDGEMENTS

TABLE OF CONTENTS

LIST OF TABLES

LIST OF FIGURES

LIST OF SYMBOLS AND ABBREVIATIONS

<u>ABBREVIATIONS</u>

MGD	Million Gallons per Day
MSF	Multistage Flash Distillation
RO	Reverse Osmosis
MED	Multi-effect Distillation
MVC	Mechanical Vapor Compression
ED	Electrodialysis
CDI	Capacitive Deionization
DO	Dissolved Oxygen
EDL	Electric Double Layer
GCS	Gouy-Chapman-Stern
mD	modified Donnan
iCDI	inverted-Capacitive Deionization
eCDI	enhanced-Capacitive Deionization
MCDI	Membrane assisted-Capacitive Deionization
eV-CDI	extended voltage- Capacitive Deionization
SAC	Salt Adsorption Capacity
SAR	Salt Adsorption Rate
E_{PZC}	Potential of Zero Charge
BET	Brunauer-Emmett-Teller
SSA	Specific Surface Area
POM	Polyoxymethylene
CV	Cyclic Voltametry
EIS	Electrochemical Impedance Spectroscopy
ACF/ACC	Activated Carbon Fiber / Activated Carbon Cloth
SHE	Standard Hydrogen Electrode

FT	Flow-through
FB	Flow-by
ppm	parts per million

SYMBOLS

$C(x)$	Concentration (as a function of distance)
$C_{salt,mA}$	Bulk Ion Concentration
Z_j	Ionic Valence
$\phi(x)$	Relative Dimensionless Potential
σ	Charge Density
λ_d	Debye Length
ϕ_d	Diffuse Layer Voltage
F	Faraday's Constant
$\varepsilon_r \, \varepsilon_o$	Dielectric Permittivity of Water
A_s	Electrode Surface Area
C_{st}	Stern Layer Capacity
ϕ_{st}	Stern Layer Voltage
V_T	Thermal Voltage
V_{cell}	Applied Voltage
Λ	Charge Efficiency
$\dot{V}$	Volumetric Flow Rate
C_{in}	Ion Concentration (at cell inlet)
C_{out}	Ion Concentration (at cell outlet)
M_{mol}	Molar Mass
m_{carbon}	Mass of Electrode Material
I	Current
Q	Charge Passed
E^0	Reference Voltage

P_a	Partial Pressure (of the gas)
k_H	Henry's Law Constant
C_a	Concentration (of the gas)
E_{charge}	Energy Consumed in Charging (the cell)
C_{charge}	Cost of Charging (the cell)
P_{pump}	Power Supplied (to the pump)
ρ	Solution Density
g	Acceleration (due to gravity)
h	Hydrostatic Head Pressure
η	Pump Efficiency
E_{pump}	Energy Consumed (by the pump)
C_{pump}	Cost (to power the pump)
t_{op}	Time of Operation
t_{life}	Cell Life
x_{carbon}	Price of Carbon (per gram)
C_{carbon}	Cost (of the carbon)

1. Introduction

According to the US Geologic Surveys of 2000 and 2005, the United States alone used around 348,000 MGD (Million Gallons per Day) of fresh water, with about 140,000 MGD for use in thermoelectric cycles (1, 2) as a cooling agent for heat rejection occurring in the cooling tower(s) and wet desulfurization device(s). Although consumption had decreased by the 2010 survey, it was still around 306,000 MGD for total fresh water usage (3). As discussed by Anderson et al. (4), only 0.006417% of earth's water is easily accessible fresh water making this a valuable resource that must be controlled and replenished as water demand continues to rise. Currently, multistage flash distillation (MSF) and reverse osmosis (RO) are the two most competitive options for water desalination but they require extensive energy in the form of either temperatures or pressures, respectively. For instance, RO and MSF require 2.9-3.7 kWh/m^3 and 4 kWh/m^3 to treat sea water respectively, and these energy values are about four times the thermodynamic minimum value for desalination of sea water (approximately 35,000 ppm) according to Anderson et al. (4). Some other desalination options currently in use throughout the world include mechanical vapor compression (MVC), electrodialysis (ED), and multi-effect distillation (MED) which preceded MSF and differs in system layout. Each of these technologies is industrially viable, but they also have high energy requirements associated with them as well.

Capacitive deionization (CDI) is a developing water desalination technology that provides energy savings in comparison to contemporary desalination technologies such as multistage flash distillation (MSF) and reverse osmosis (RO) when treating brackish-level

(1000 ppm to 5000 ppm) streams (4, 5). CDI functions by using an applied voltage to electrostatically adsorb ions in solution onto pairs of electrodes, such that the ionic salt species in solution are attracted to the electrodes of opposing polarity until the electrodes become saturated. For concentrations at or below brackish levels, CDI could be competitive with RO and MSF in terms of energy consumption, even if charge-discharge cyclic efficiencies as low as 60 to 70% are assumed (4).

This thesis discusses capacitive deionization, detailing the many variations in design and operation that can have an effect on performance. In particular, the work presented here is in response to a noticeable lack of adsorption capacity as well as performance decay via extensive degradation of the anode (positive electrode) in the presence of dissolved oxygen coupled reactions (6). Both of these features hinder the progression of CDI towards commercialization. Recent works have explored in detail the influence of dissolved oxygen (DO) on CDI degradation and performance (7, 8). In summary, cathodic DO reduction and anodic carbon oxidation form a redox pair in competition for the electrical driving force imposed on a CDI cell. Products from the reaction can include hydrogen peroxide, which can further exacerbate electrode degradation (9, 10).

Theorizing that the interaction between the saline solution and the carbon-based electrodes could be obstructed by trapped air, and noting that a main component of performance degradation is electrode oxidation, the effect of applied pressure across the cell was investigated for this dual purpose. This pressurization theory follows Henry's law, which states that at a given temperature, the amount of dissolved gas in solution is proportional

2

to the partial pressure of the gas at its interface with the solution. The application of pressure with Henry's law implies that trapped gasses in the pore space of the electrode material could be compressed, dissolved, and carried out of the cell in solution and subsequently released upon exiting the pressurized portion of the system. Figure 1.1 illustrates the effect that additional pressure has on gases trapped in the electrode's pore space while Figure 1.2 demonstrates the pressure induced increase in solubility of gasses according to Henry's law. If pressurized operation positively influences adsorption capacity and degradation rate, is it plausible in keeping with the low cost benefits presented by capacitive deionization despite the increased pumping cost? This question will be investigated throughout this thesis.
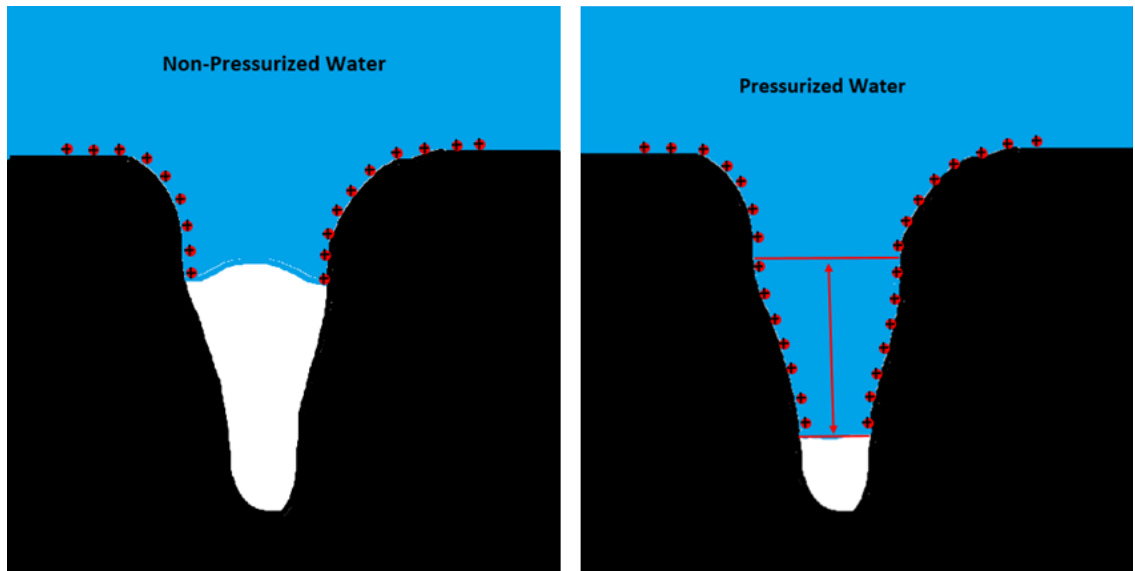
Figure 1.1. Illustration of how compressing gasses could allow the solution to contact more of the electrode's surface area.
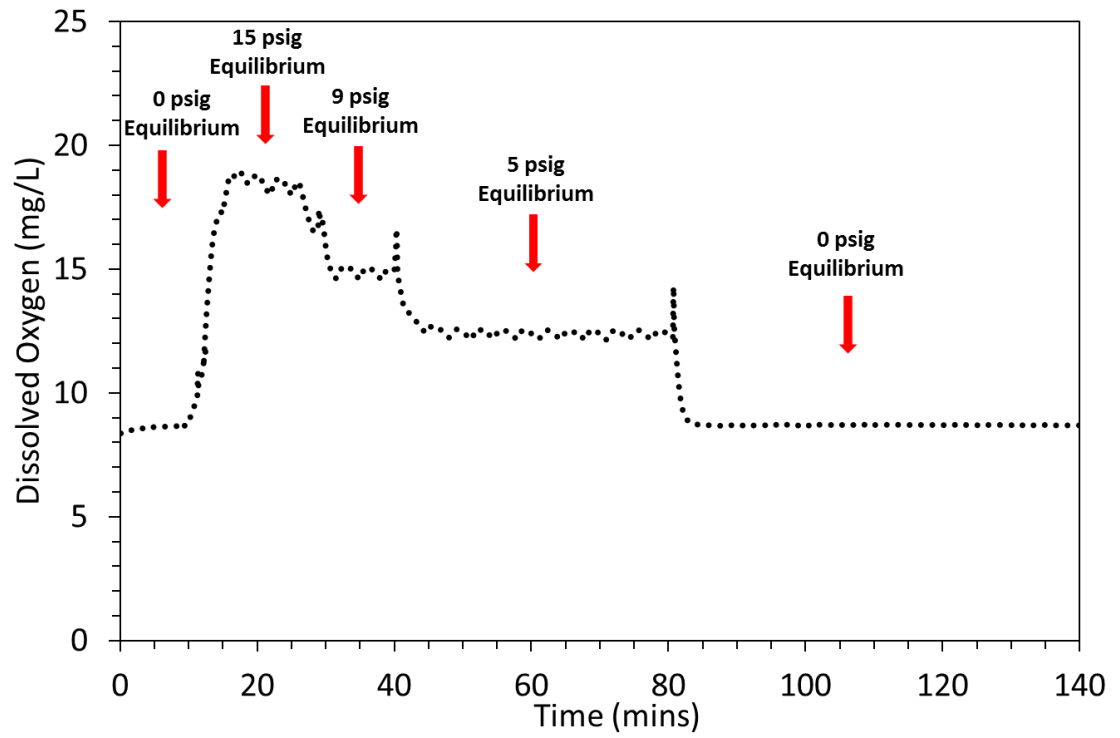
Figure 1.2: Preliminary data illustrating Henry's law with dissolved oxygen in the solution as a function of pressure and time.

2. Background and Literature Review

2.1. What is CDI and How Does It Work

In conventional CDI technology, a small voltage, typically <1.5 volts, is applied across pairs of the porous electrode material. The resulting electric field acts as the driving force behind dissolved ions coming out of solution and electrostatically collecting in the electric double layer (EDL) that forms near the surface of each polarized electrode, similar to the way supercapacitors store electrical charge. The applied potential along with some chemical surface charges, inherent to the electrode material, together move ions toward the counter-charged electrode, and this accumulation of ionic charge compensates for the potential difference, which has been applied externally to the electrodes. Just as a supercapacitor, storing electrical charge, eventually reaches a maximum capacity, so do CDI electrodes storing ionic charge. Once the storage capacity is reached and adsorption stops; the electric potential is removed, typically through a physical short-circuit of the electrodes, and the ions to diffuse back into solution. Figure 2.1 demonstrates how the capacity of an electrode pair is reached based upon the current passed between the electrodes acting as the driving force behind ion adsorption. In order to maximize adsorption, or salt adsorbed per mass of adsorbent material, most electrodes are carbon based. This selection is due to the high surface areas, achieved through activation processes, and low activity for water splitting that carbon has to offer (6, 11). Despite the extremely high surface areas of the activated carbon electrodes commonly used, typical CDI adsorption capacities only utilize a small percentage of this surface area (6). Specific details, provided later in this chapter, discuss how the addition of backpressure and

dissolution of trapped gasses attempt to free up some additional adsorption sites / active surface area.
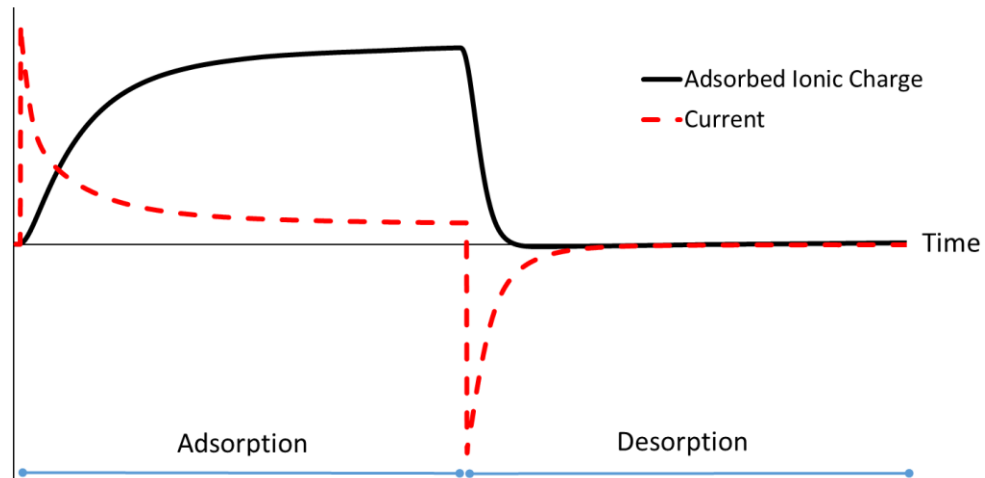
Figure 2.1: Current driven ion adsorption and desorption where the delayed response from the adsorbed charge is due to conductivity probe placement after the cell in the flow. Note: The non-zero current remaining at the end of the adsorption phase drives the inevitable degradative (Faradaic) reactions.

2.1.1. Fundamentals of the Electric Double Layer (EDL)

Some common models used to describe the EDL phenomenon include the Helmholtz model, the Gouy-Chapman-Stern (GCS) model, and the modified Donnan (mD) model. The Helmholtz model assumes that charge is distributed on the entire surface of the electrode and all adsorbed counter-ions reside in a plane near the surface of the electrode material compensating for the opposite electrical charge built up there. This implies an efficiency of 100% or the ideal situation for CDI (11). In reality, ions are held both in a plane near the electrode's surface, and in a diffuse matrix that is also near the surface of the electrode where co-ion repulsion occurs in addition to counter-ion adsorption.

This understanding is modeled by the GCS model, which is a combination of the diffuse layer (Gouy-Chapman model) and the Helmholtz plane. The area between the electrode and Helmholtz plane is known as the Stern layer, as Otto Stern incorporated the two models into the single Gouy-Chapman-Stern model. In the GCS model, the Stern layer is separated from the diffuse layer by the Helmholtz plane, or the plane of closest approach. Thus, the thickness of the Stern layer corresponds to the radius of the hydrated ions. The diffuse layer, separated from the carbon by the Stern layer, does not maintain a set thickness; rather, the ion concentration decreases with increasing distance from the electrodes' surfaces. The GCS model also accounts for the potential of co-ion desorption giving it more realistic efficiencies, with respect to experimental data, and is provided in Equations 2.1-2.6 (11). However, neither of these models completely describe the EDL structure with respect to typical CDI electrode geometries and porosities. The Helmholtz model fails in assuming unity efficiency from the lack of co-ions. The GCS model fails when electrode geometry constraints cause diffuse layer overlap (12). Porada et al. (11) states that the GCS model, developed for planar electrodes, is only applicable to macroporous carbons where the EDL is thinner than the electrode's pore radius. In this case, the ion concentration at a distance x from the electrode's surface is given as

$$C(x) = C_{salt,mA} * e^{-Z_j * \phi(x)} \tag{2.1}$$

where $C_{salt,mA}$ is the bulk ion concentration, Z_j is the ionic valence, and ϕ is the dimensionless potential relative to the that in the neutral bulk solution.

The GCS model assumes ions are point-charges, where integration over the diffuse layer provides the surface charge density as σ in Equation 2.2 (11).

$$\sigma = 4\lambda_d C_{salt,mA} * \sinh\left(\frac{1}{2} * \Delta\phi_d\right)$$ [2.2]

In Equation 2.2, ϕ_d is the diffuse layer voltage and λ_d is the Debye length given by Equation 2.3,

$$\lambda_d = 1 \Big/ \sqrt{\frac{2F^2 C_{salt,mA}}{\varepsilon_r \varepsilon_o RT}}$$ [2.3]

where $\varepsilon_r\varepsilon_o$ is the dielectric permittivity of water, F is Faraday's constant, R is the universal gas constant, and T is the temperature.

Additionally, from Equation 2.1, we can solve for the salt adsorption capacity (SAC) as a function of electrode surface area, A_s (13) which is given as Equation 2.4.

$$SAC = 8\lambda_d C_{salt,mA} * sinh^2(\frac{1}{4} * \Delta\phi_d) * \frac{A_s}{2}$$ [2.4]

Finally, the complete GCS equilibrium must consider the Stern layer voltage ϕ_{St} related to the charge σ, the thermal voltage V_T (approximately 25.7 mV at room temperature), and C_{st} the Stern layer capacity in F/m^2. as shown in Equation 2.5, and the relationship to the applied voltage V_{cell} shown in Equation 2.6.

$$\sigma * F = C_{St} * \Delta\phi_{St} * V_T \qquad [2.5]$$

$$\frac{V_{cell}}{2 * V_T} = |\Delta\phi_d + \Delta\phi_{St}| \qquad [2.6]$$

A diagram outlining the GCS model can be seen in Figure 2.2. Although the GCS model leads to over-estimated adsorption capacities compared to more advanced models like the mD model (4), the GCS model provides the basis from which other models were formed and demonstrates the importance of the effective surface area which led to this backpressure study attempting to increase the performance through surface area utilization.
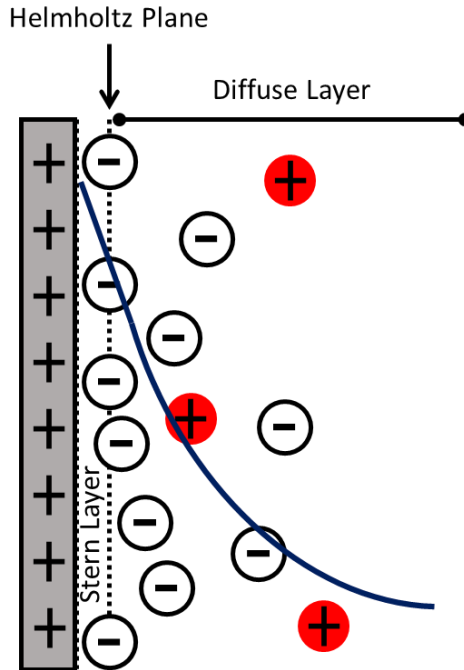
Figure 2.2: Illustration of the GCS model.

2.1.2. System & Cell Components

All CDI systems must include a power source for applying a potential difference, electrodes as adsorption media, some instrumentation providing a separation performance metric, and a pump or other mechanism for moving the water and/or electrodes with respect to each other. The most common CDI experimental setups, demonstrated by Figure 2.3, employ a pump to transport saline water from a reservoir to a cell enclosing static electrodes and back to a reservoir (6, 14-16). Additionally, the most common instrumentation used to track performance are inline conductivity meters digitally logging the effluent conductivity throughout the cell's charge and discharge cycles.
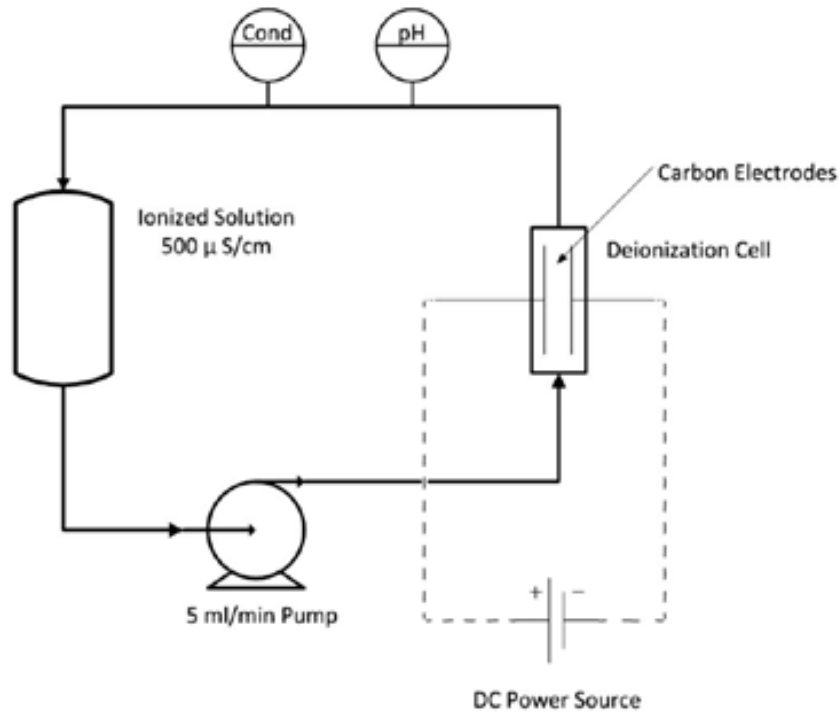
Figure 2.3: Schematic of common CDI system (6).

This system structure generally desalinates a feed stream in two stages with intermittent deionized water production. In the first stage, while a voltage/potential is applied, the electrodes remove ions from solution and the effluent is collected as the deionized stream. In the second stage, the electrodes, now at capacity with adsorbed ions, are physically short circuited removing the electrostatic force constraining the adsorbed ions. These ions, no longer held to the electrodes, desorb into the solution flowing through the cell creating a concentrated stream. This is collected as waste or reintroduced to the bulk, before the inlet to the system, for testing purposes. The two steps of this operation are shown in Figure 2.4.
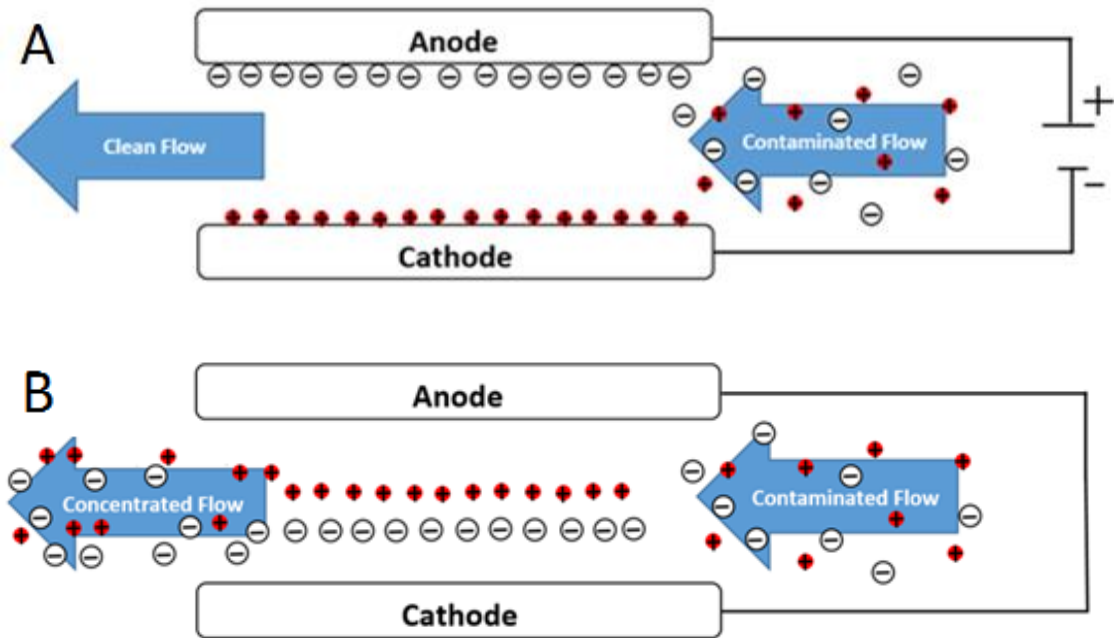
Figure 2.4: CDI operation (A) Adsorption stage, (B) Desorption stage.

As previously stated, there are many system designs for capacitive deionization. One other variation of CDI employs static saline solutions and transports the electrodes between them, called desalination with wires, in the form of switch wheel (11). Another utilizes flowing saline solution and a flowing electrode slurry, called flow-CDI (12). Desalination with wires utilizes thin carbon rods as electrodes, that while located in the deionizing reservoir, have a voltage applied across them adsorbing ions until they reach their adsorption capacity. At this saturation point, the rods are transferred to the concentrating reservoir where they are physically short circuited, depositing the previously adsorbed ions into the concentrated reservoir. In this manner, the desalinated reservoir would ideally contain a much larger volume than the concentrated reservoir thus increasing the water recovery of the system (11). In contrast, flow-CDI utilizes a slurry-based electrode where the influent saline solution can undergo continuous desalination because the flowing

electrode-slurry is replenished outside of the desalination cell through a separate process (12). There are many types of CDI systems that each accentuate different performance characteristics. In addition, there are also many cell design variations for each type of system as well.

Although there are many ways to design a CDI cell, just as with the entire system, there are certain components that allow it to function as intended. The reversible electro-adsorption of ions requires that the ions periodically experience an electric field in addition to having room on the electrodes to which they will adsorb. Thus, in addition to the electrode material, all CDI cells must electrically isolate the cathode from the anode and provide proper contact between each electrode and the source applying potential between them. Therefore, the cell components that must be present in the cell in some form include the electrode material, a current collector, and a cathode-anode electrical separator that does not hinder the fluid's interaction with the electrode. As stated previously, electrode materials are commonly carbon-based due their high surface area and low propensity for water splitting. In addition, for the separator material, it is important to have electrical inertness with a low flow resistance, and for the current collector material, it is important to have high electrical conductivity as well as corrosion resistance. Figure 2.5, shows a simple cell structure that demonstrates the placement of these components within the CDI cell. More details on material selection are discussed in Section 2.3.
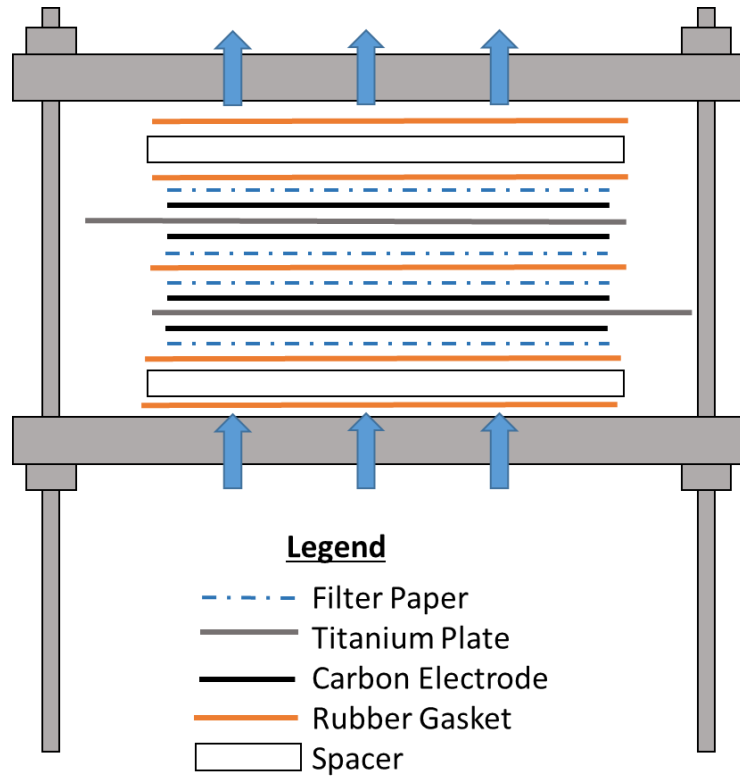
Figure 2.5: Simple CDI cell structure showing component placement within.

2.2. History of Capacitive Deionization

Capacitive deionization, although still an emerging technology, is not a new idea as research in the area dates back to the early 1960's when the concept was first studied. A combination of work from Porada et al. (11) and Oren (5) provide the history of CDI and the major influencing contributions since its birth in 1960. Some of the pioneering contributions made were by J. W. Blair, G. W. Murphy, S. Evans, W. S. Hamilton, D. D. Caudle, and A. M. Johnson, along with their associated groups. The following paragraphs will discuss in more detail the early discoveries in the field of electrochemical deionization and the developments that led to the present understanding of CDI.

The concept, derived in 1960, was termed electrochemical demineralization of water. When first studied by Blair and Murphy, they believed that the driving forces were specific surface chemical groups, which would oxidize or reduce leading to their bonding with the ions in solution (11). In the mid 1960's, Evans and Hamilton joined in using Coulometric and mass balances to evaluate the demineralization ability of carbon electrodes. They believed that cathodic polarization of the carbon electrode drove Faradaic reactions producing OH^-, which would create acidic surface groups to bind with sodium ions while an anodized silver electrode would lose electrons and gain chloride ions. Upon reversing the polarity of the two electrodes, Faradaic reactions producing H^+ would create an environment favorable for the reformation of the acidic surface groups and the release of the sodium ions while the anodized silver electrode would gain electrons and release the chloride ions. Here, efficiency was calculated based on the coulomb equivalent of ions removed from solution to the coulombs passed through the electrodes (17). By 1969, Evans and Accomazzo had changed from the single carbon electrode to two carbon electrodes, pretreated differently, where one electrode reacted with sodium ions and one reacted with chloride ions each through Faradaic reactions. Subsequently, adjusted efficiency calculations were then the ratio of ion concentration to the calculated value based on Faraday's law (18). Additional driving discoveries made in the late 1960's, include one by Reid et al., that other ionic species such as calcium, magnesium, sulfate, and nitrate could also be removed from solution through electrochemical desalination (11).

In the early 1970's, Johnson et al. derived a new theory for the desalination mechanism termed "Potential modulated ion sorption". This theory is consistent with the Electric

Double Layer theory (EDL), which is considered as the true mechanism behind the electrochemical desalination of water. In addition, the Faradaic reactions, previously believed to be the driving mechanism, were determined nonessential and can even lead to electrode degradation and performance loss (10, 11, 14, 19-21). Potential modulated ion sorption theory states that at the interface of electrodes and an electrolytic solution there is a region on the electrode, not charge neutral, that is balanced by an excess of oppositely charged ions in solution (22). Johnson and Newman then showed that this mechanism could be accurately modeled as a combination of resistances and capacitances as opposed to the series of chemical reactions modeled by Faraday's law (23). This theory also allowed a cost evaluation that demonstrated the industrialization potential for capacitive deionization through a competitive cost around 22 cents to desalinate one-thousand gallons from 1760 ppm of NaCl to less than 500 ppm (22), this is equivalent to $1.41 per 1000 gallons in 2017 when accounting for inflation. Further contributions by Johnson et al. determined that the capacity of the electrodes is a function of the electrical capacity of the EDL, the available surface area of the electrodes, and the voltage applied to the cell (11). The work of Johnson and his associates led to vast amounts of research on the fundamental understanding of capacitive deionization (5). One of the final works in the late 1970's was the development of "electrochemical parametric pumping" (24), which was a modified version of parametric pumping, a thermal separation method developed in 1966 utilizing a packed bed of adsorbent particles (25). Electrochemical parametric pumping utilized a four-step process. Step 1: Applied potential adsorption, step 2: forward flow, step 3: reverse potential desorption, and step 4: backward flow. This process was an attempt to enhance

the concentration gradient between the dilute and concentrated solutions by minimizing mixing that occurs in the absence of flow reversal (24).

Around the end of the 1970's capacitive deionization saw a reduction in research that lasted until the 1990's when it regained focus, specifically in the area of electrode development. One of the most notable was the development of the carbon aerogel by Pekala et al. (26). Due to its pore structure, high surface area, and high conductivity, carbon aerogel was considered a progression from the previously used activated carbon (11). Many other electrodes have been developed since but carbon aerogel is still widely used today (27-30). Developments in CDI since the 1990's are discussed in the remainder of this thesis and include areas such as operating conditions and cell design which, for the purpose of this thesis, are considered current, as opposed to historical, developments.

2.3. Cell Design & Operation

Proper material selection for cell components, the arrangement of these components within the cell, and the mode under which the cell operates are of critical importance if a CDI design is to be commercially viable (5).

For the electrodes, there are many carbon-based materials to select from where the main variations between them are pore size, structure, and surface condition. The most common electrode materials include activated carbon fibers/cloths, carbon aerogels/xerogels, and other various nano-porous carbons (4, 12, 31, 32). A comprehensive list detailing the extent

of the different material's use can be found in Table 2.1 below. These materials are popular due to commonly agreed upon properties including high surface area to mass ratio, high electronic conductivity, fast response through fast ion mobility in the pores, high (electro)chemical resistance over wide voltage and pH ranges, high biofouling/scaling resistance, and easy formability to fit cell dimensional requirements (5, 11).

The separators isolating the oppositely charged electrodes must be electrically insulating, yet they must also be open-structured as to not hinder the bulk flow through a high pressure-drop. These characteristics lead different forms of filter paper or polymeric materials to be commonly chosen for this component. On the other hand, current collectors need high electrical conductivity and must be resistive to corrosion and biofouling because the ionic solutions treated induce corrosion and may contain organic contaminants. Considering these characteristics, common current collector materials include titanium (5, 14, 27, 30, 31, 33), and graphite (14-16, 21, 34-37).

Table 2.1: Research Efforts Employing Specific Carbons.

Carbon Type	Research Effort Utilizing the Material	
Aerogel/Xerogel*	Suss et al.	(27)
	Qu et al.	(38)
	*Landon et al.	(6, 39)
	*Gao et al.	(33, 40, 41)
	*Omosebi et al.	(42)
	Shapira et al.	(43)
	Noked et al.	(44)
	Xu et al.	(30)
	Gabelich et al.	(29)
	Pekala et al.	(26)
Activated Carbon Fiber/Cloth (ACF) / (ACC)	Huang et al.	(45)
	Bouhadana et al.	(14)
	Cohen et al.	(16, 46)
	Avraham et al.	(15, 36, 47-49)
	Shapira et al.	(43)
	Noked et al.	(44)
	Gao et al.	(50, 51)
	Omosebi et al.	(52)
	Ryoo et al.	(53)
Various Other Nano-porous Carbon	Porada et al.	(35)
	Kim et al.	(34, 54)
	Hou et al.	(55)
	Li et al.	(56)
	Nie et al.	(57, 58)
	Pan et al.	(59)

2.3.1. Cell Structure

Listed above are common electrode materials, but more detail will be given in later sections as to the differences. These details will lead us to the preferable arrangement of the cell's components. There are many cell structures that orient the components differently. As mentioned previously, there are some designs that require the movement of the electrodes from one body of water to another, but for the purpose of this thesis, those designs will be disregarded as they are much less common than cells where the fluid is transported around

stationary electrodes. The two basic cell structures for stationary electrodes include flow-through (FT) and flow-by (FB), referring to the orientation of the solution with respect to the electrodes. In both cell structures, the cathode and the anode, coupled with current collectors, are stacked parallel to each other, typically separated by a porous filter paper of some sort for their electrical isolation, and these stacks can contain a single pair of electrodes or multiple (11).

Flow-by structured CDI cells direct flow perpendicular to the electric field, between parallel pair(s) of oppositely charged electrodes. This flow path depends on the diffusion of ions for electro-static adsorption occurrence (46). This is the most widely used cell structure and has been used in many works including those by Blair and Murphy in 1960 as well as by Oren's group in the 1980's and Farmer's group in the 1990's (12). Flow-by cells typically employ either an open flow channel around 1 mm thick or utilize the porous separator between the electrodes, typically 100 to 300 μm thick, as the flow channel. Additionally, the flows are usually not one-dimensional, rather the cell geometry sets the flow path as radially inward/outward, or from one edge of a rectangular channel to the edge on the opposite corner (11). A schematic showing the flow orientation of flow-by cell structures can be seen in Figure 2.6 below. In addition to the pioneering groups that used flow-by structured cells, Table 2.2 below lists research groups that typically employ them versus those that typically employ flow-through cell structures.
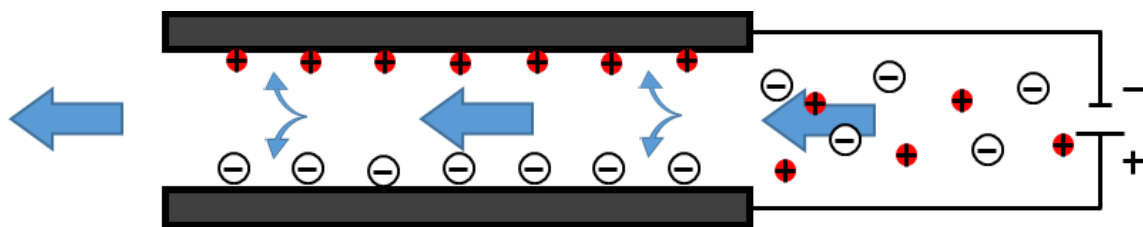
Figure 2.6: Diagram illustrating flow orientation of the saline solution with respect to the electrode pair in a flow-by structured cell.

Flow-through CDI cells direct the hydraulic flow through the face of the stacked electrodes aligning it parallel with the electric field (12). This requires that the flow passes through the macropores of the electrodes minimizing the role of diffusion in the electro-adsorption of ions (46). In comparison to flow-by cells, flow-through CDI cells are historically associated with a fast desalination rate due to the flow of the solution being directed perpendicular to the face of the electrodes (parallel to the electric field) as opposed to along the surface. This orientation allows the solution to directly interact with the electrodes by relying on solution flow instead of ion diffusion to achieve ion proximity with the electrode surface (11, 27). The limited dependence on ion diffusion and the freedom to decrease/eliminate the spacer thickness between electrodes, allows flow-through CDI cells to have a faster response to the applied potential as well as stronger reductions from the feed solution concentration (12, 27).

The issue with flow-through cell designs is that the solution interacts with only one electrode at a time, either the cathode or the anode. This in-turn leads to local pH swings (as charge balance) during adsorption and when aided by faradaic reactions, e.g. oxygen reduction at the cathode, associated with a locally high pH, leads to enhanced oxidation of the anode (9, 21). The flow path, interacting first with the cathode, carries the reaction

products directly to the anode thereby enhancing the pH-dependent carbon oxidation reaction. This differs from flow-by CDI cell designs where the flow path runs parallel to the face of the electrodes, and the reaction products from the cathode do not directly interact with the anode, where the most significant degradation occurs (43, 46).

Flow-through cell structures were first explored by Johnson et al. in the 1970's, and were then also utilized much later by Avraham et al. in the early 2000's. Since the early 2000's, this design has become much more prevalent. A schematic showing the flow orientation of flow-through cell structures can be seen in Figure 2.7 below along with the list of research groups that have utilized the structure in Table 2.2. In this thesis, the differences between flow-through and flow-by cell structures will be further investigated, with regard to the effect that the structure has on the CDI performance.
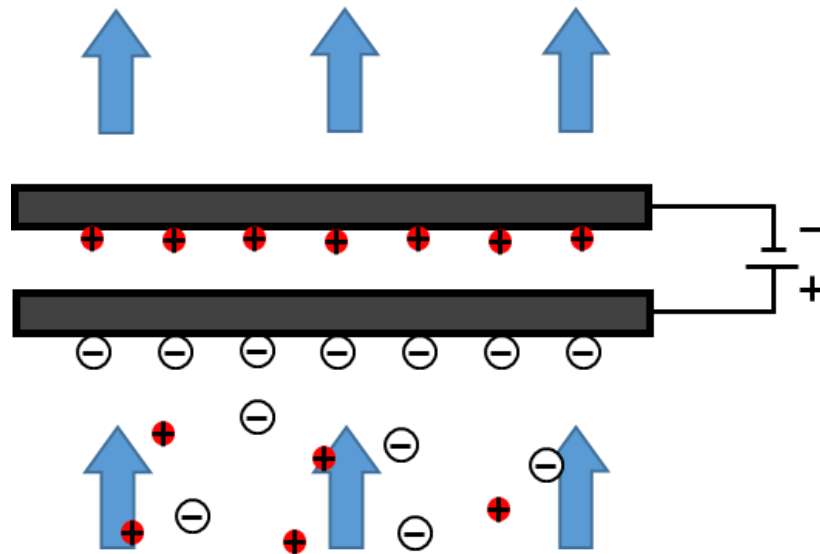
Figure 2.7: Diagram illustrating flow orientation of the saline solution with respect to the electrode pair in a flow-through structured cell.

Table 2.2: Research Efforts Employing Specific Cell Structures

Cell Structure	Research Effort Utilizing the Structure	
Flow-Through	Cohen et al.	(16, 46)
	Avraham et al.	(15, 36, 47-49)
	Qu et al.	(38)
	Landon et al.	(39)
	Gao et al.	(33, 40, 41, 50)
Flow-By	Cohen et al.	(46)
	Porada et al.	(35)
	Kim et al.	(34)
	Huang et al.	(45, 60)
	Bouhadana et al.	(14)
	Landon et al.	(6)

2.3.2. Modes of Operation

The final aspect of CDI cell design that must be determined is the mode of operation. The mode of operation signifies the driving force behind ion removal and if the driving force is assisted by ion selective membranes that improve performance and reduce electrode oxidation. Carbon-based electrodes used in CDI operation are considered pristine in the as-received condition. Beyond this, electrodes can be subjected to pretreatment (before CDI implementation) in either amine/acid solutions or oxidized through deionization operation introducing net positive or negative chemical surfaces charges, depending on the method, on the electrode's surface and inside the pores (51). A deionization system or process implementing pristine anodes and cathodes, from here on, will be termed CDI. When utilizing pretreated carbon materials, or oxidized spent electrodes, for either the cathode, the anode, or both; the system or process is termed inverted-CDI (iCDI) or enhanced-CDI (eCDI) with the differentiation discussed later in this section (41, 51). The presence of ion selective membranes in a CDI system allocates it as membrane assisted-CDI or an (MCDI)

system. Although ion selective membranes can be implemented in iCDI and eCDI systems (42), for the scope of this review, MCDI will only be discussed in reference to its application where both the cathode and anode are pristine.

As described earlier, CDI uses an applied electrical field between electrodes to attract and adsorb salts dissolved in solution. During the charging step, performance degradation occurs in the form of anode oxidation forming COO^- functional groups, due to the carbon reacting chemically with the water or dissolved oxygen. The oxides that form give the anode a negative chemical surface charge, which hinders CDI desalination performance. Due to this oxidation and accumulation of chemical surface charge, the ratio of counter-ion adsorption to co-ion desorption decreases, with the implication that larger potentials are now needed to force a net removal of ions from solution. Gao et al. (41) discuss how this accumulation of chemical charge on the electrode, can be utilized as the driving force to chemically adsorb ions from solution, as opposed to the use of an electrical driving force. This phenomenon is called inverted-CDI or iCDI because, as shown in Figure 2.8, the desalination step occurs during the absence of the applied potential under a physical short circuit. Additionally, the charging phase is the concentrating phase where the applied potential neutralizes the chemical charge releasing the ions back into solution. Interestingly, the stability of iCDI is much greater than CDI, with cell operation for over 600 hours being demonstrated by Gao et al. (41).
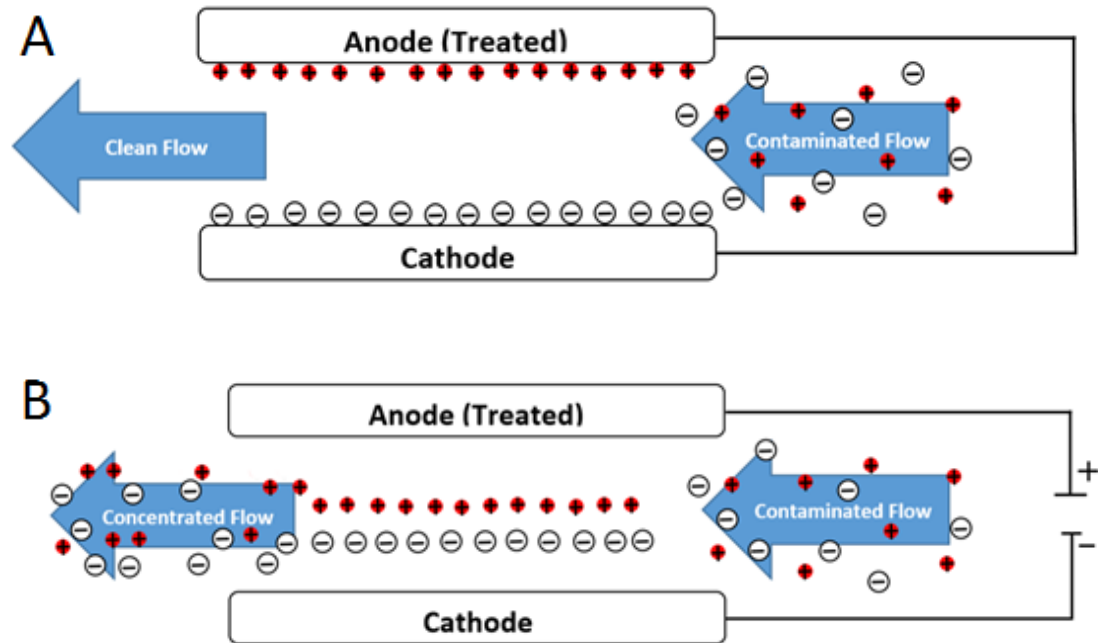
Figure 2.8: iCDI operation (A) Adsorption stage (B) Desorption stage

The direction of the applied voltage with respect to the electrodes' asymmetric surface charges determines the difference between iCDI and eCDI. As stated above, when the anode (positive electrode) is the pretreated (oxidized) electrode, the applied potential neutralizes the adsorption-driving chemical force causing desorption of the ions previously adsorbed. When the cathode (negative electrode) is the acid treated or oxidized electrode it is considered in eCDI mode. The addition of applied potential, negative at the cathode, to the negative chemical charge at the cathode, increases the adsorption capacity of the electrode, which now attracts ions using both chemical charge and the applied potential as driving forces for desalination.

This mode of operation, depicted in Figure 2.9, is improved by the additional chemical surface charge as opposed to hindered by, as is the case with CDI. This is because in CDI

the chemical charge is opposite of the applied potential, thus attracting co-ions which must be repelled by the applied potential. In eCDI the chemical charge has the same sign as the applied potential and thus natively repels co-ions (11). Less co-ion repulsion by the applied potential means that the number of the electrons passed between electrodes compared to the number of ions removed from solution becomes closer to a one-to-one ratio. This increased capacity is demonstrated by Gao et al. (51) and can be accurately modeled by a modification of the Donnan model called the amphoteric-Donnan model.
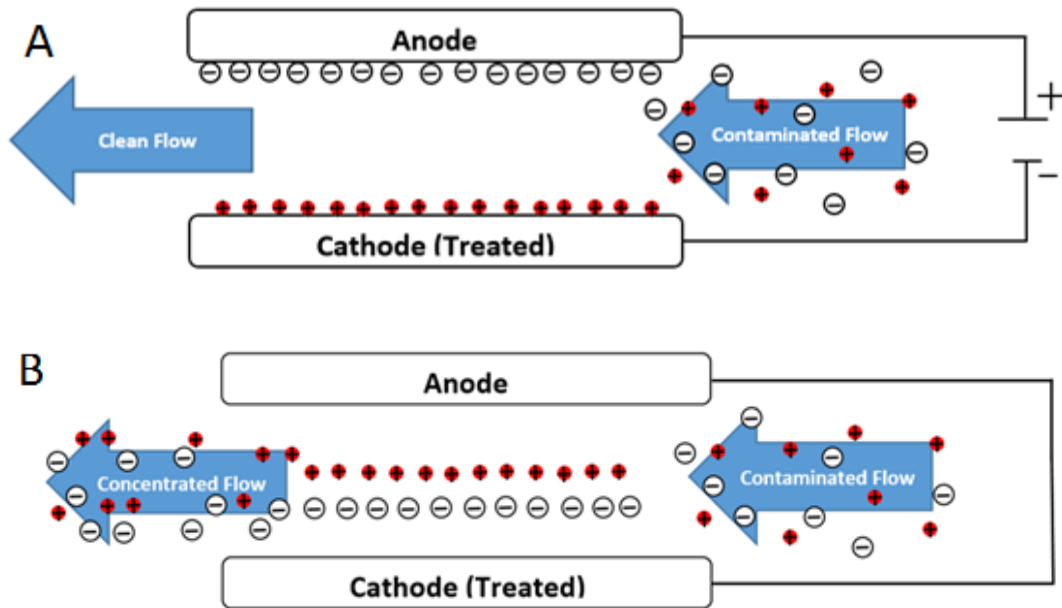
Figure 2.9: eCDI operation (A) Adsorption stage (B) Desorption stage

As mentioned above, electrodes treated in acid solutions form negatively charged surface groups while those treated in amine solutions form positively charged surface groups. The pretreatments shift the electrodes' potential of zero charge (E_{PZC}) towards more positive and negative potentials, depending on the process. A combination of an acid and amine

treated electrodes thus, expands the working voltage window two-fold, further increasing the desalination capacity of the cell. Additional increases in capacity are depicted by the amphoteric-Donnan model when the applied voltage to an eCDI cell is properly distributed. This allows it to be larger without restriction from water splitting (51). This implies that instead of operating at 1.6 volts and a short circuit, operation at ± 0.8 volts. This operation has been termed extended voltage CDI (eV-CDI), and is also demonstrated by Gao et al. (51) to be in accordance with the amphoteric-Donnan model.

One final mode of operation includes the addition of ion selective membranes between the carbon electrodes in the alternating CDI stack. The charging and discharging phases of operation for an MCDI cell are identical to those for a CDI cell, but provide an increased adsorption capacity for similar reasons as eCDI. As described by Omosebi at al. (52), the ion selective membranes are asymmetric and must be placed in front of the correct electrode. Convention in CDI dictates the anode as the electrode that attracts anions and the cathode as the electrode that attracts cations because it is based on the charging step as opposed to the ion discharge with batteries and supercapacitors (4, 11, 12). Anion-exchange membranes must pair with the electrode attracting anions, which for CDI is the anode or positive electrode. Likewise, cation-exchange membranes must pair with the cathode or negative electrode. The reason for specific placement is due to the polar driving forces behind adsorption. If a membrane is on the wrong electrode, it will counteract the adsorption driving force at the electrode, thus causing significantly reduced adsorption capacities. This effectively eliminates co-ion desorption, drastically increasing the

efficiency and capacity of the cell. A schematic of an MCDI cell can be seen in Figure 2.11 below.
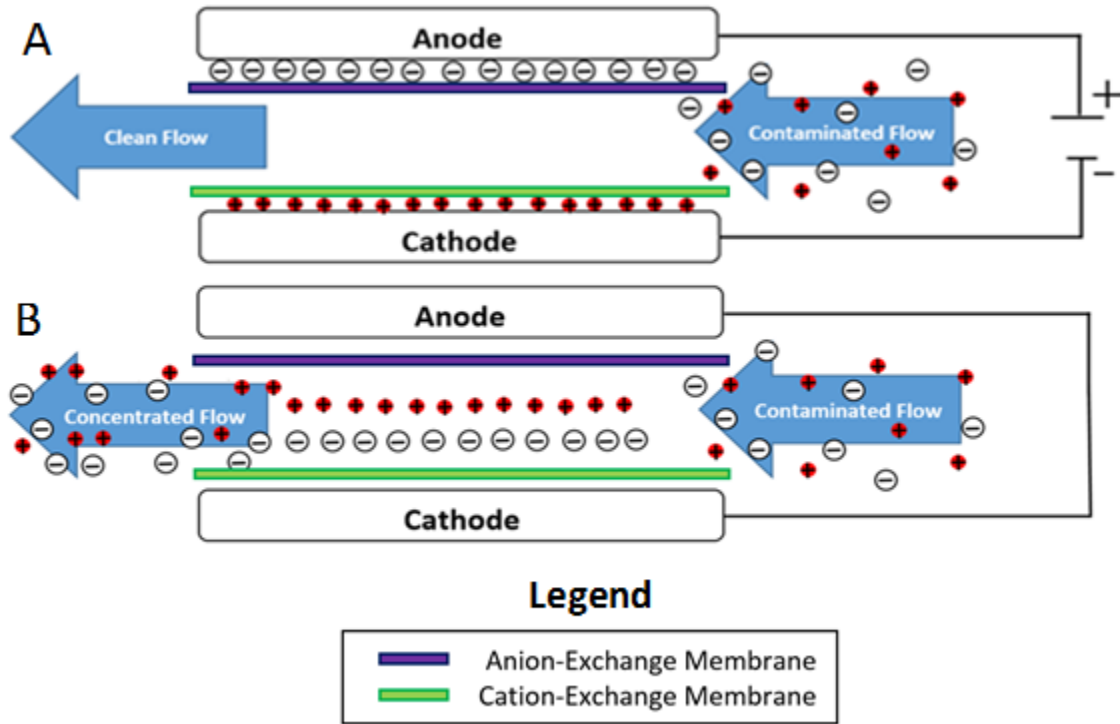
Figure 2.10: MCDI operation (A) Adsorption stage (B) Desorption stage, where the anodic and cathodic ion-exchange membranes are in purple and green respectively.

An additional benefit to MCDI is that many ion-exchange membranes inhibit the transport of dissolved oxygen in the bulk stream from reaching the electrodes. This feature of the membranes is especially useful as dissolved oxygen is a key reactant in the reactions that degrade the performance of the cell through increasing electrical resistivity, surface chemical charging, and loss of active surface area (52).

2.4. Metrics for Performance

2.4.1. Primary Metrics

Important metrics for the performance of a CDI system include the primary metrics: salt adsorption capacity (SAC) (23, 31, 32, 38, 48, 50, 61), salt adsorption rate (SAR) (23, 31, 32, 38, 44), and charge efficiency (Λ) (23, 31, 32, 45, 47, 48, 50, 61). These metrics are typically evaluated on a cycle to cycle basis but can also be integrated over sub-cycle time scales for more specific comparisons between cells.

The SAC is defined as the mass of salt adsorbed in a single cycle normalized by either the mass or the volume of the electrode material in the cell. By integrating the concentration difference between the inlet and outlet of the CDI cell over the charging cycle and plugging it into Equation 2.7 with some cell and operation parameters, you will arrive at the salt adsorbed in mg/g of electrode, or the gravimetric SAC, shown below (12, 34). Alternatively, dividing by the volume of the electrode instead of the mass, you can arrive at the volumetric SAC in mg/m3.

$$SAC = \frac{\dot{V} * \int (C_{in} - C_{out}) * M_{mol} * 1000(\frac{mg}{g})}{m_{carbon}} \qquad [2.7]$$

In this equation, $\dot{V}$ is the volumetric flow rate (L/hr), C is the ion concentration (mol/L), M_{mol} is the molar mass of the dissolved ionic compound (58.44 $\frac{g}{mol}$ for NaCl), and m_{carbon} is the mass of the electrode material (g). As a side note, due to measuring

equipment, concentration (mol/L) must be calculated from conductivity (μS/cm), where accurate conversion requires a calibrated conversion specific to the conductivity probe(s). The SAR is simply calculated by dividing the SAC by a time interval, typically the total charging time; however, this time interval can be the charge length or any shorter time interval to compare a more instantaneous rate of adsorption with units given in (mg/g/min) (12).

The final primary metric is the charge efficiency (Λ), which is unit less (Coulombs/Coulombs). Charge efficiency is defined as the ratio of SAC equivalent charge to the charge passed between electrodes or the current integrated over time. In Equations 2.8 and 2.9, shown below, I is the current, Q is the charge passed between electrodes, and F is Faraday's constant (41).

$$Q = \int I * dt \qquad\qquad [2.8]$$

$$\Lambda = \left(SAC * \frac{F}{M_{mol}}\right)/Q \qquad\qquad [2.9]$$

2.4.2. Secondary Metrics

Metrics for more specific CDI performance are here termed secondary metrics as they are derived from the primary metrics. The two most common include a combined comparison of SAC and SAR through the ragone plot (12, 31, 34, 54, 62, 63), and also the degradation rate, or rate that the SAC decreases from cycle to cycle (16, 27, 41, 42, 46, 64, 65).

The ragone plot, termed the Kim-Yoon plot for CDI systems, displays the SAR versus the SAC, both on log base 10 scales. In this format SAR and SAC changes, with respect to each other, allow a more in depth comparison of CDI performance, on the scale of a single cycle or between multiple cycles. Figure 2.12 illustrates a ragone plot's basic interpretation (34).
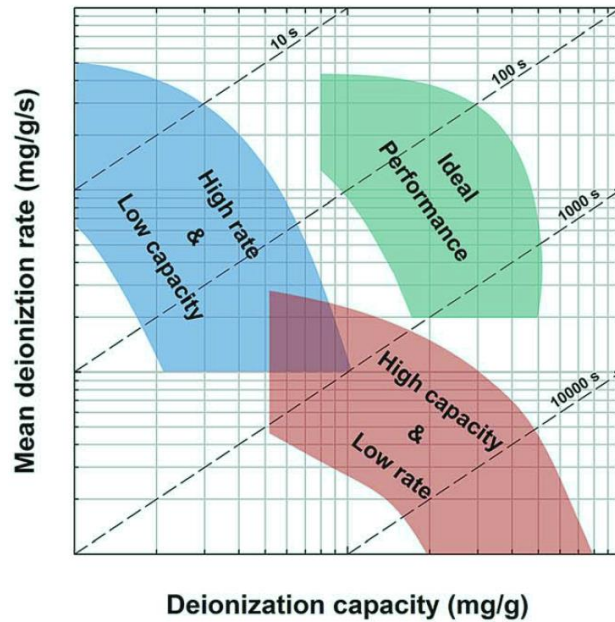
Figure 2.11: Basic interpretation of ragone plots on a single cycle scale (34).

The rate of degradation, another secondary metric, can be tracked a couple of ways. The most general method is to inspect the SAC or charge efficiency and see how quickly they decrease from their initial levels, which provides an accurate depiction regardless of the mode of operation. In the case of CDI (cells utilizing pristine electrodes) degradation is coupled with anode oxidation and a shift of the electrode's potential of zero charge (E_{PZC}) as depicted in Figure 2.12.
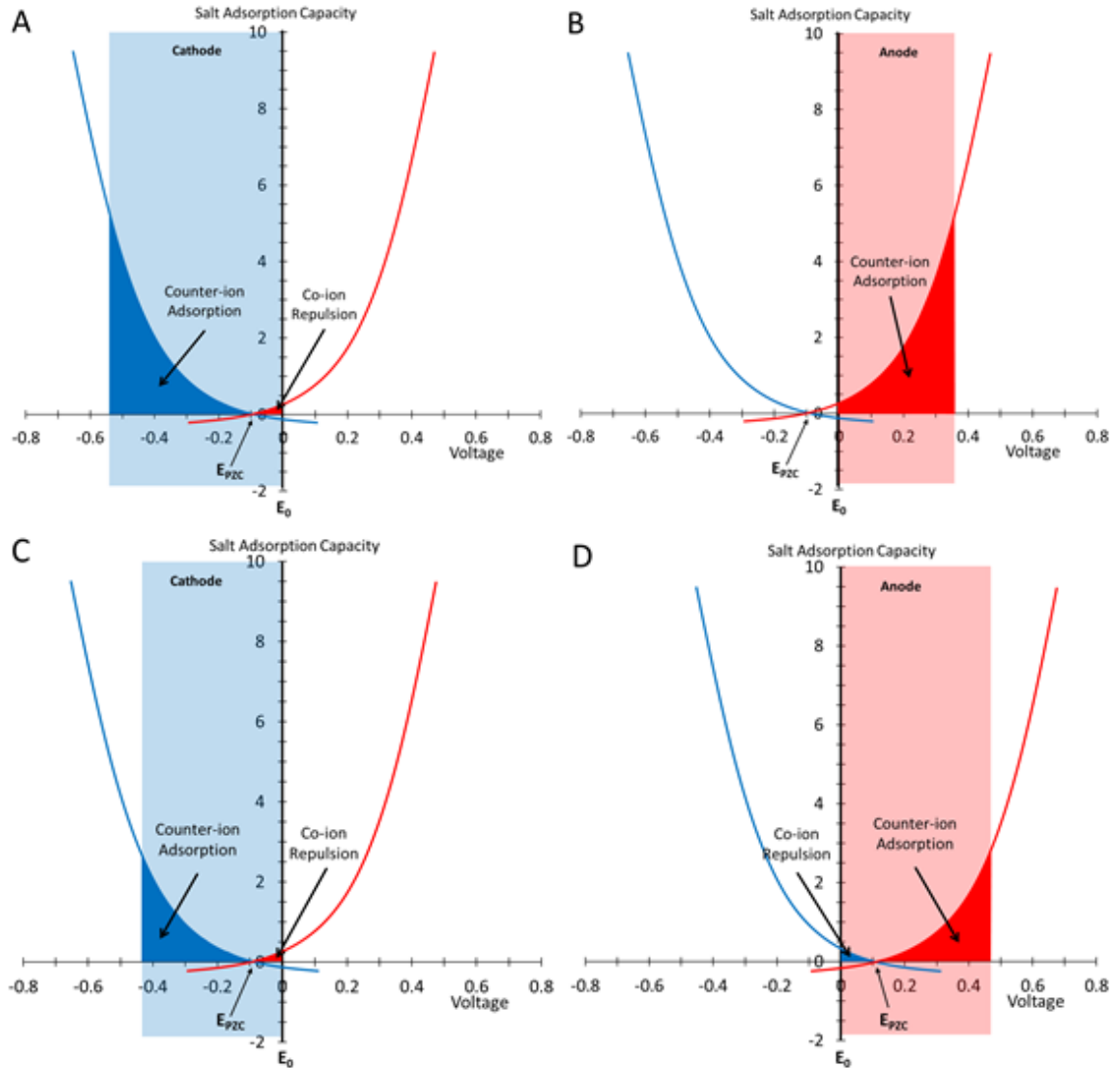
Figure 2.12: Example of E_{PZC} location for (A) pristine Kynol ACC from the cathode's perspective, and (B) pristine Kynol ACC from the anode's perspective. The E_{PZC} locations for degraded electrodes are shown in (C) the cathode's un-shifted E_{PZC} location and (D) the anode's shifted E_{PZC} location. Additionally, note that the uneven potential distributions also shift due to the shifting E_{PZC} of the anode.

As the E_{PZC} of anode shifts, due to the accumulation of chemical surface charge described in Section 2.3.2, co-ion repulsion increases and eventually appears in the conductivity profile as a small desorption spike at the beginning of each charge cycle (10, 33, 65). This inversion spike continues to grow as the anode degrades until it reaches a point where

desorption and adsorption occur equally within a single charging stage. From this point on, if the cell potential is lowered to allow full desorption events under potential and full adsorption events under short-circuit conditions, the cell is considered to be in iCDI mode. The point of inversion is a milestone in the cell's life and thus the rate of degradation can also be described in terms of the number of cycles before inversion occurs (16, 33, 46, 50).

Some additional information on degradation can be drawn from the voltage and current profiles, specifically the leakage current (9, 10, 41). The voltage and current profiles provide information on the mechanisms of degradation, faradaic reactions. Faradaic reactions, pertinent to CDI, can be broken down into three categories: oxygen evolution/reduction (19), carbon oxidation (42, 50, 66), and hydrogen evolution (19) which are shown respectively in Equations 2.10 - 2.12.

$$O_2 + 4H^+ + 4e^- \rightarrow 2H_2O \quad E^0 = 1.23 \ V/SHE \qquad [2.10]$$

$$C_{surface} + H_2O \rightarrow C = O_{surface} + 2H^+ + 2e^- \\ E^0 = \sim 0.704 \ to \sim 0.904 \ V/SHE \qquad [2.11]$$

$$2H^+ + 2e^- \rightarrow H_2 \quad E^0 = 0 \ V/SHE \qquad [2.12]$$
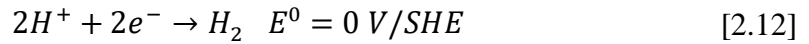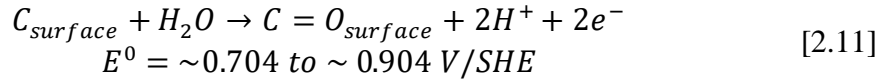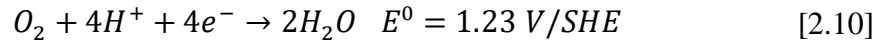
Another indication of degradation that can be used is pH, local to the electrodes' surfaces, due to the faradaic reactions causing the production of H^+, and OH^- for balancing charge distributions within the solution (11). Although voltage, current, and pH trends are indicative of degradation, they are not individually conclusive. Additionally, many aspects in CDI cell design and operation play a role in the desalination performance of the system. The most prevalent of these aspects are discussed in the remainder of this chapter.

2.5. Factors that Influence Performance

2.5.1. Factors Commonly Monitored

There are many factors that affect the performance metrics discussed in the previous section. In order to achieve repeatable performance from any type of CDI system, these factors must be monitored and kept consistent. Operation parameters like solution concentration, flow rate, applied voltage, and cell packing density along with electrode properties like thickness and pore size / surface area are the most common factors monitored across all CDI platforms. Each of these factors influences desalination performance independently; therefore, in controlled experimentation, they must be kept constant unless they are the variable of focus.

Consider the salt adsorption rate of a CDI system. SAR has a positive correlation with all of the system parameters: solution concentration (34, 44), flow rate (34), applied voltage (12, 27), packing density (12, 35), and all of the electrode properties thickness (12, 34, 35), pore size / surface area (5, 6, 12, 35, 44), making this the most widely affected metric. The capacity of CDI operation is another metric widely affected by these system and electrode parameters. SAC has a positive correlation with applied voltage (12, 27), the electrode's pore size / surface area (5, 6, 12, 35, 44, 45), and with solution concentration, at lower salinity levels (34, 44). Charge efficiency is closely tied to the SAC, increasing with applied voltage increases (12, 45) but is affected inversely by solution concentration increases due to the potentially increased presence of co-ions (5, 12). The final performance metric mentioned, degradation rate, is not affected by as many of the common system parameters.

Of the common factors mentioned, the applied voltage (41, 43) is the only one commonly associated with degradation; however, although less commonly monitored in general, dissolved oxygen levels in the influent stream also play a large role in degradation as mentioned in the previous section.

2.5.2. Electrode Material/Pores (Size / Space / Availability)

As previously mentioned, most electrode materials are carbon based due to their high surface area to mass ratio, which is due to substantial microporosity. In addition to surface area, pore size and pore distribution play major roles in the performance of the electrodes in CDI applications. Typical specific surface area (SSA) seen in carbon based electrodes range from 100's (m^2/g) to 1000's (m^2/g) measured using nitrogen adsorption/desorption isotherms and calculated using Brunauer-Emmett-Teller theory (BET) (6, 11, 36). BET specific surface area (BET SSA) measures all pores including interparticle and intraparticle pores with sizes ranging from micropores to macropores. See Figure 2.13 below for pore nomenclatures (11).
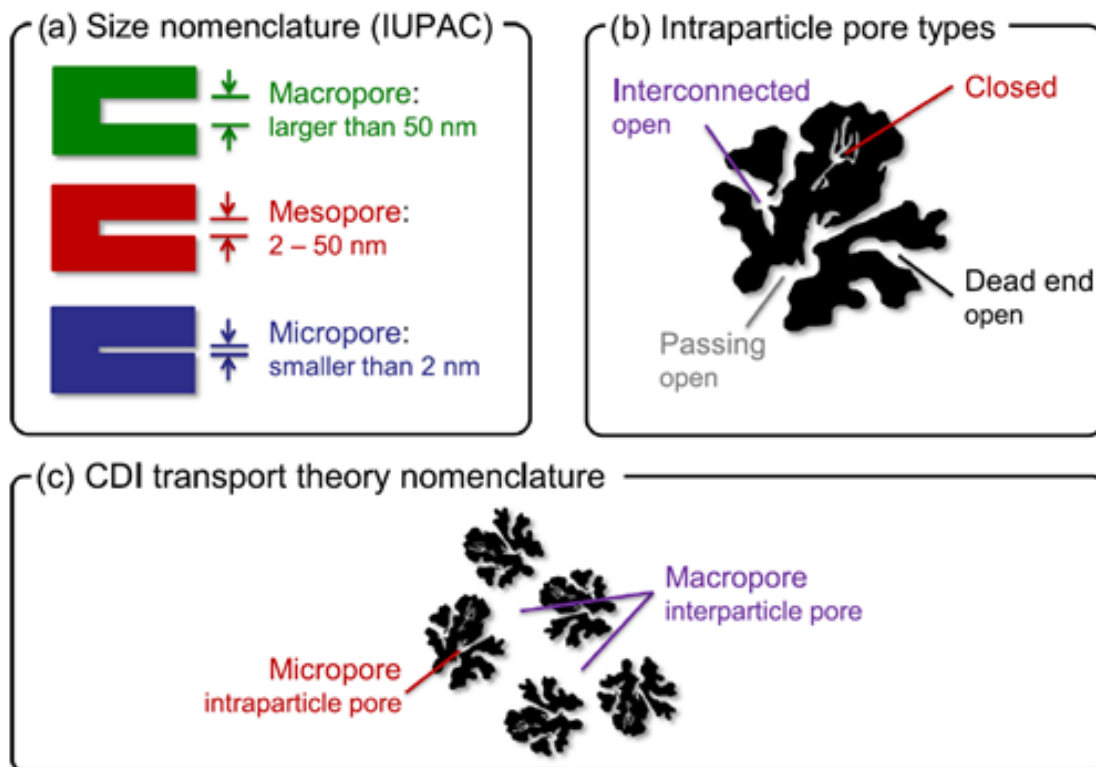
Figure 2.13: Pore size and type nomenclature (11).

Although BET SSA provides a ranking of SSA, it does not accurately describe the SSA available for ion adsorption. An N_2 gas molecule has a radius of 0.155nm, which is smaller than even monovalent Na^+ or Cl^- ions, which have hydrated radii of 0.358 and 0.311 nm respectively. Thus, BET SSA is typically much larger than the SSA actually available for salt adsorption (4-6). Generally, as BET SSA increases, the pore size decreases. Although increased surface area correlates with increased SAC, decreasing pore size correlates with decreasing SAR and poor surface area utilization. This even extends to a point where pores below a certain size could be too small for adsorption to occur at all (6, 16, 44, 45, 67). Thus, in order to accurately predict the adsorption capacity of an electrode, one must consider the pore size distribution and the ratio between pore size and hydrated counter ion

size in addition to SSA. These aspects help account for the adverse effects of increasing surface area through decreasing pore sizes (6, 11, 16, 45).

2.6. Research Question

Regardless of surface area or pore volume, the capacity of carbon electrodes remains fairly consistent. Despite the large specific surface areas that the carbons boast, if the surface area used for adsorption is calculated from the mass of salt adsorbed, less than 15 m^2/g SSA is needed, which is 10% or less of the BET SSA of most carbon based electrodes (6). This leads to the question that drove the research presented in this thesis: How to increase utilization of the electrode's surface area?

As mentioned in the introduction and displayed in Figure 1.1 and 1.2 we believe that the addition of back pressure on the CDI cell can increase the surface area that is accessible to the saline solution through compression and dissolution of gasses that were not fully evacuated from the electrode's pore structure or cell's void spaces. In addition to increasing the active surface area for adsorption, the removal of oxygen from the system could also help mitigate degradation as oxygen is one of the main reactants in the faradaic reactions leading to carbon oxidation and loss of separation capability.

3. Experimental Methods

3.1. Applied CDI Methods

3.1.1. CDI System Configuration

In applying our pressurization approach to CDI operations, the following system was implemented and is shown in Figure 3.1. A positive displacement piston pump, Scientific Systems Inc. Prep 100 Legacy HPLC Pump, draws the saline solution from a reservoir, containing a minimum of 10 liters, and pumps it to the CDI cell. Following the CDI cell, ¼ in. tubing leads to two small reservoirs containing a Eutech Instruments C621-2-1-1 Conductivity Cell, and a Eutech Instruments 971651 In-line Dissolved Oxygen Probe. An MC Daniel Inc. 316SS, 0-200 psi, pressure gauge and GO Inc. SP3-1A11B51114, 0-250 psi, pressure regulator immediately follow these measurement probes. After the solution exits the regulator and the pressurized portion of the flow loop concludes, there is a pH probe, Cole-Parmer Solution Grounded pH Probe, DJ/PPS/100Ohm RTD. This probe is outside of the pressure loop due to limitations in operable pressure range. Each of the measurement probes is read by its appropriate transmitter, Eutech Instruments: Alpha COND 500 (ECCONCTP0500), Alpha DO 500 (35151-10), and Alpha pH 500 (ECPHCTP0500); data logging from these probes takes place every 5 seconds by a Graphtec midiLOGGER GL240 (GL240-UM-850) data logger and is subsequently exported to an excel file for data analysis. After exiting the pH probe, the solution returns to the reservoir, which is bubbled with air to insure the DO level is constant at ambient saturation for its eventual reintroduction to the cell. A second DO probe, placed in the

reservoir, displays this DO content, where the bubbled air also ensures enough fluid flow across the probe tip for an accurate reading.
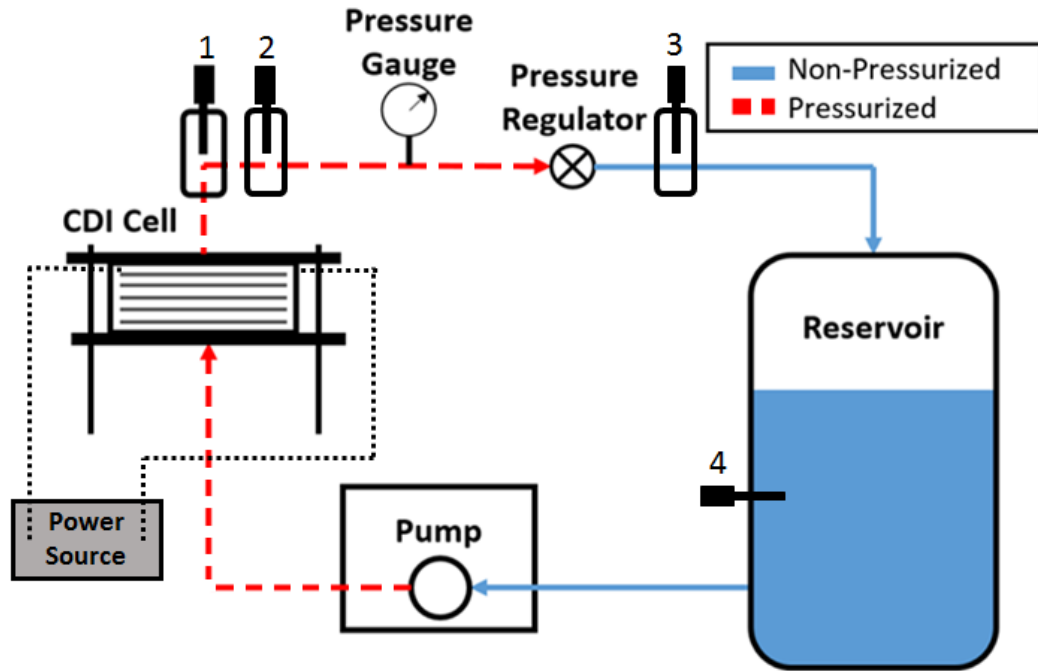
Figure 3.1: Diagram of the CDI system components where measurement probes, numbered 1-3, include the conductivity probe, dissolved oxygen probe, and the pH probe respectively, where the 4th probe is an additional dissolved oxygen probe ensuring a constant DO level enters the system.

3.1.2. Flow-Through Cell Architecture

The flow-through CDI cell implemented in this study contained five pairs of pristine, as received, activated carbon cloth, provided by Nippon Kynol. Each electrode was 4.75 in.^{2} with a mass of approximately 0.4 g for a total electrode mass of around 4 g per cell. The carbon was electrically isolated by sheets of Whatman Qualitative Grade 4 filter paper. The applied electric potential was supplied by an Aligent E3632A power supply connected with

18-gauge wire with Dexmet 100 LF MicroGrid titanium mesh acting as the current collector. Additional filter paper and a 1/8 in. thick porous diffuser were placed at the inlet to the cell to ensure even flux of solution across the entire surface of the electrodes. All of these cell components were contained within a 9/16 in. thick polyoxymethylene (POM) shell compressed at the top and bottom by 1/16 in. thick silicone gaskets and 18-8 stainless steel plates, each with three ports to allow the solution in or out of the cell. The steel plates, compressed to 0.475 in. of separation, created the seal essential for containing the pressurized saline solution. A diagram and photo of the flow-through cell design implemented in this study are shown in Figure 3.2.

Legend

�(blue)	POM Shell
– · – · –	Filter Paper
——— (gray)	Titanium Mesh
——— (black)	Carbon Electrode
——— (orange)	Rubber Gasket
XXXX	Porous Diffuser
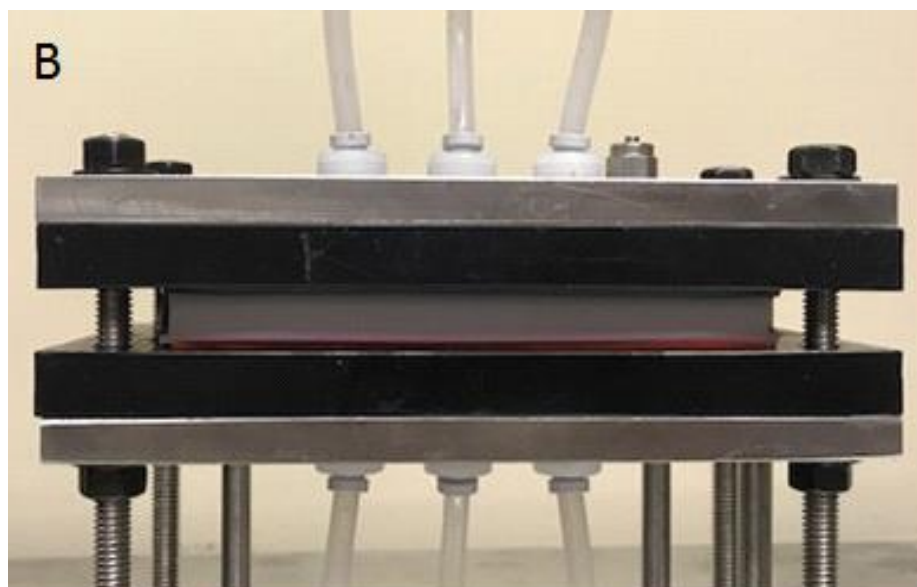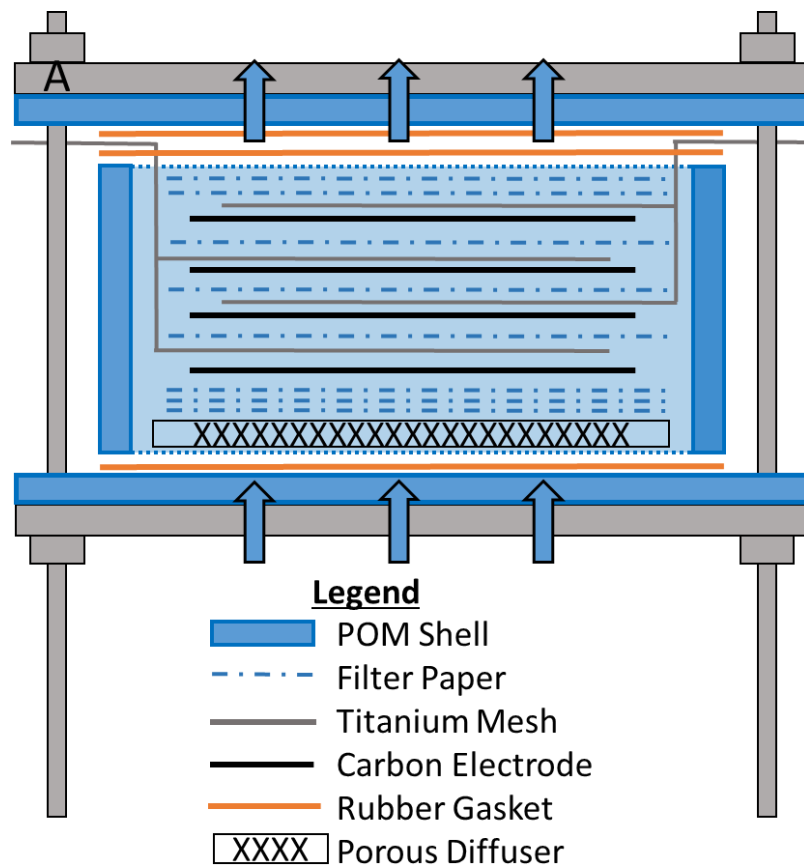
Figure 3.2: Flow-through CDI cell structure (left) where arrows represent the inlet and outlet ports connected to ¼ in. tubing. A photo of the constructed flow-through cell (right) displays the cell used in experimentation.

3.1.3. Flow-By Cell Architecture

The flow-by CDI cell utilized in experimentation included 3 pairs of pristine, as received, activated carbon cloth, provided by Nippon Kynol. Each electrode was 4.87 in.^{2} with a mass of approximately 0.43 g for a total electrode mass of around 2.6 g per cell. Two sheets of Dreamweaver polymeric separator around plastic mesh created a path for solution flow between the oppositely charged electrodes, while keeping them electrically isolated. The current was supplied to the electrodes by the same Agilent E3632A power supply and 18-gauge wire; however, the current collectors were made of 1/16 in. titanium sheet metal. In flow-by cells, flow is directed between the electrodes instead of through them, so the current collectors are solid and non-porous to ensure that flow follows the correct path as demonstrated in the flow-by diagram (left) in Figure 3.3. To ensure even dispersal of the solution across the width of the flow path, a 3/8 in. thick POM spacer allowed the solution to spread to the correct width before entering the flow channel and the first electrode. Similarly, before exiting the cell, an identical POM spacer was used to ensure that flow did not stagnate anywhere inside the flow channel. All of the cell components were compressed to 0.86 in. by the same 9/16 in. thick POM shell and 18-8 stainless steel plates, with 1/16 in. thick silicone gaskets between each current collector and spacer to create the seal essential for containing the solution under pressure.
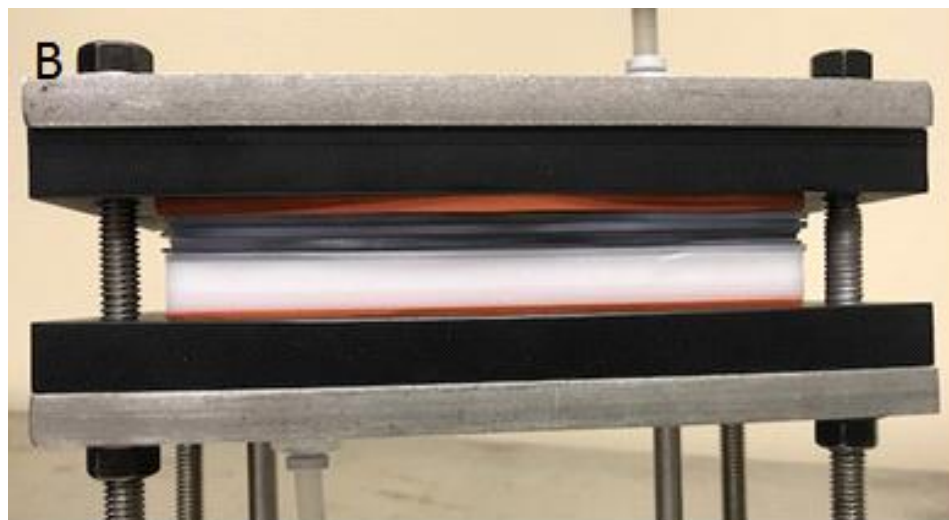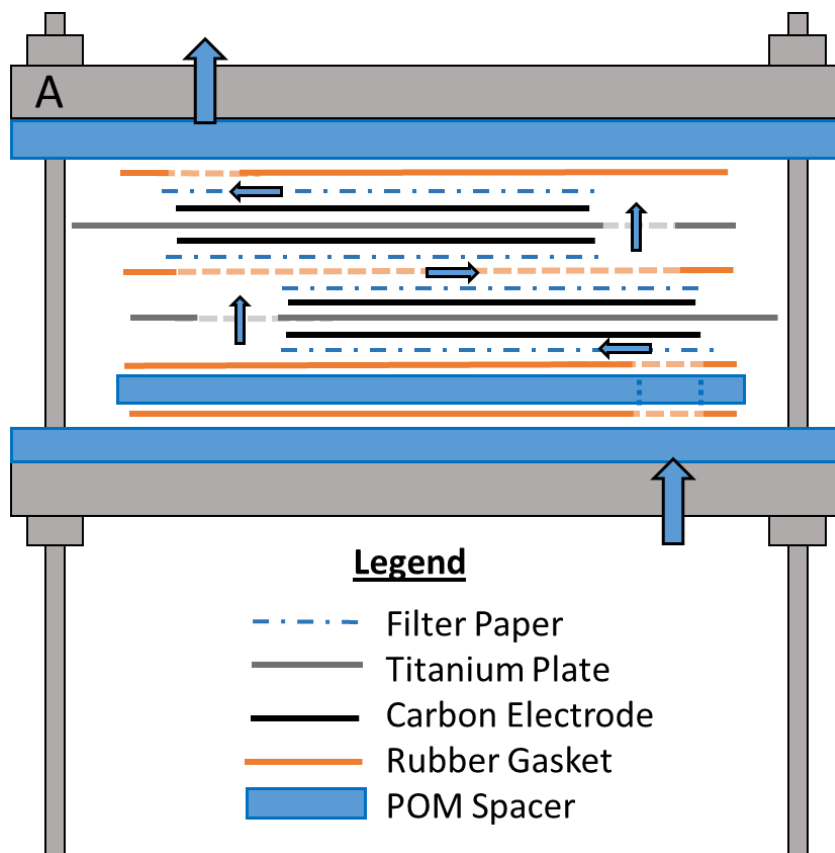
Figure 3.3: Flow-by CDI cell structure (A) where arrows represent the inlet and outlet ports as well as the flow path within the cell. A photo of the constructed flow-by cell (B) displays the cell as used experimentation.

3.1.4.   Operational Parameters

The CDI cells, described above, were operated under a constant voltage of 0.9 V for one hour and were subsequently discharged, by physical short circuit, for another hour, giving a complete cycle time of two hours. A saline solution, containing 5 mM sodium chloride, was fed through the system at a constant 16 mL/min. Two backpressure conditions, 0 psig and 60 psig, were tested, where the flow resistance caused by the flow traveling through the electrodes and filter paper gives an additional pressure drop of 1 psig across the cell.

Prior to cell assembly, the electrodes were wetted in 5 mM sodium chloride solution for the dual purpose of ease of assembly and ensuring maximum wetting of the electrodes for the most consistent baseline of non-pressurized electrodes possible. Additionally, upon inserting the cell in the system, the cell was introduced upside-down into an increased flow of solution (approximately 30 mL/min) to expel air bubbles from any larger voids at the cell's inlet. Once the cells were filled with the saline solution, they were manually agitated until gases were no longer seen exiting (approximately 1-2 minutes). At this point, the cells were removed from the flow path and placed right side up where gravity would keep any voids filled with solution while flow was restored. Once gases were no longer seen exiting the cells in this orientation (approximately 1-2 minutes), the flow was reduced to 16 mL/min, which concluded system preparation.

3.2. Post Examination of Electrodes

During CDI operation, faradaic reactions irreversibly alter the carbon electrodes, specifically the anode where the most degradation occurs (43, 46). This irreversible change can be seen in the shift of the electrodes' potential of zero charge (E_{PZC}) at which the least ions are adsorbed. Determining the electrodes' E_{PZC} can be accomplished through a cyclic voltammetry (CV) experiment (33, 36), through the immersion method (15, 16), or through electrochemical impedance spectroscopy (EIS) (42, 52). The significance of the E_{PZC} location is that a shift in the positive direction can be explained by the carbon oxidation, Equation 2.11, and accumulation of chemical surface charge that occur as a result of applied potential in aqueous solution (15, 16, 33).

3.2.1. Cyclic Voltammetry

Using CV to determine the E_{PZC} location requires the use of a half-cell, which looks at the characteristics of a single electrode. Figure 3.4 shows a diagram and photo of the half-cell used for this post examination. The counter electrode ensures that the limiting adsorption occurs on the working electrode by offering an abundance of surface area in comparison to the working electrode, and for this experiment pristine Kynol ACC was implemented. The reference electrode, from which baseline measurements were taken, was a silver / silver chloride electrode. A Reference 600 Gamry potentiostat controlled the experiment, and logged voltage / current data before being subsequently exported to an excel file for analysis.
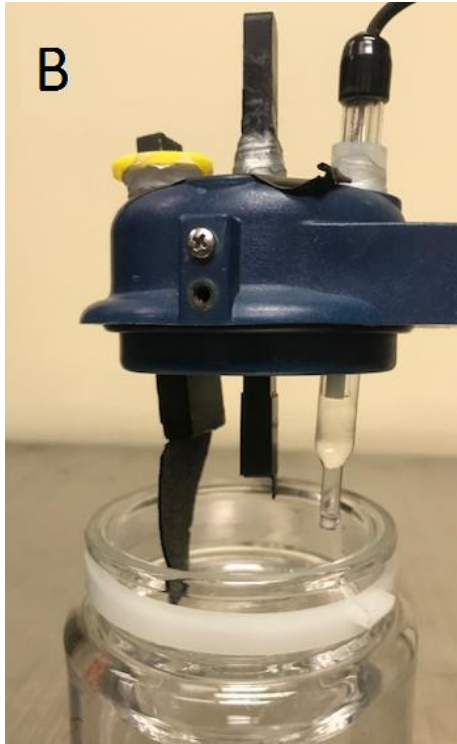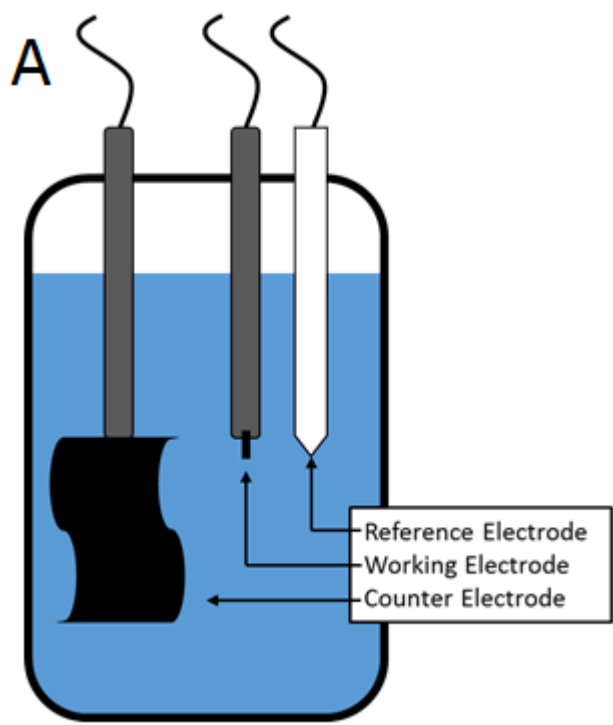
Figure 3.4: (A) shows a diagram of the half-cell used in CV experimentation, with the counter electrode (pristine Kynol), the working electrode (electrode of interest), and the reference electrode (silver / silver chloride). (B) shows a photo of the half-cell used in experimentation.

4. Results and Discussion

High concentrations of dissolved solids in industrial process water make it unlikely that CDI alone could treat the stream to a recyclable level; however, using CDI as one component of a larger series of water treatment methods is feasible. In this scenario, the salt adsorption rate of the CDI cell becomes important as to prevent CDI from becoming the rate-determining step for the entire industrial desalination process.

Experimentation began with a comparison between flow-through and flow-by cells to verify the structure best suited for industrial applications. As discussed in Section 2.3.1, flow-by cell structures rely more heavily on ion diffusion from the bulk stream to achieve ion proximity to the electrodes' pore space than flow-through cells (27, 46). The diffusion-limited adsorption of flow-by cell structures likely plays a large role in the lower SAR when compared to flow-through cell structures (27). Figure 4.1 shows a ragone plot comparing the average first cycles of CDI operation in flow-through and flow-by cells under an applied potential of 0.9 V. It is evident that the flow-through cells show a better salt adsorption rate when compared to flow-by cells under normal operation, (i.e. with no additional backpressure). These results verify that, with respect to the SAR, our flow-through cell structure would be better fit for an industrial desalination series than our flow-by cell structure. For this reason, the following pressurization experiments were conducted with flow-through cells to further optimize their use for industrial desalination purposes.
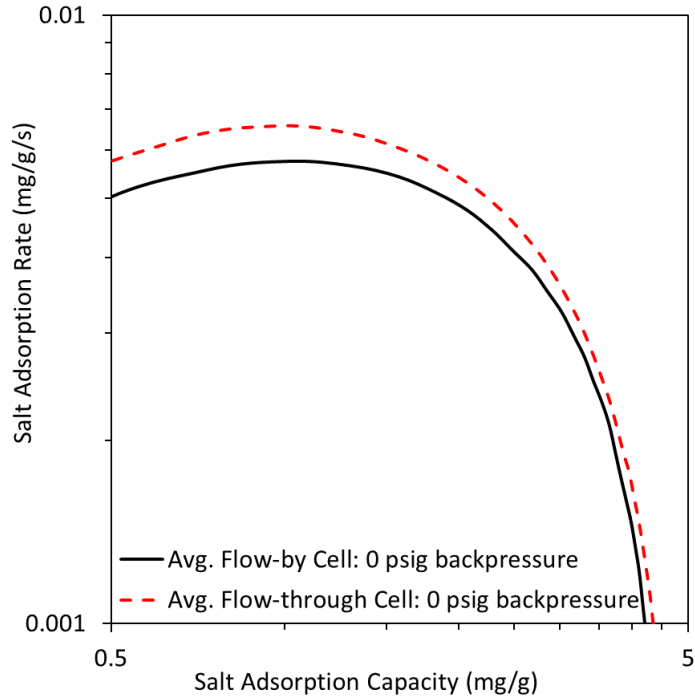
Figure 4.1: Ragone plot of CDI operation in flow-through and flow-by cell structures for the first charge cycle under an applied potential of 0.9 V and no additional backpressure.

4.1. Dissolved Oxygen and Pressure

Initial data in Figure 1.2 shows the dissolved oxygen content of our 5mM saline solution responding to changes in pressure. Table 4.1, shows the experimental values obtained in that experiment, demonstrating that the DO response to pressures is in compliance with Henry's law. Experimental values for the Henry's law constant were calculated using Equation 4.1 (68),

$$P_A = k_H * C_A \qquad [4.1]$$

where, P_A is the partial pressure of the gas at the interface with the solution, k_H is the Henry's law constant, and C_A is the concentration of the gas dissolved in solution.

Additionally in Table 4.1, these results are compared to the accepted theoretical value for the Henry's law constant for oxygen in water (69).

Table 4.1: Henry's Law Constant: Experimental and Theoretical Values for Oxygen in Water.

Gauge Pressure (psig)	Henry's Law Constant at 298 K (L*Atm / mol)
0	775.2
16	758.3
10	756.5
6	761.1
0	770.0
Average Experimental Value (All Pressures)	764.2
Theoretical Value (at 298 K)	769

Upon introduction of the CDI cell to a steady flow of saline solution, the carbon electrodes' natural affinity for oxygen is seen as the dissolved oxygen meter, placed after the cell, shows a reduced amount compared to the meter in the reservoir (e.g. the inlet solution to CDI) without applying pressure. This reduction can be chemical or physical adsorption and is solely related to the electrode material. With the application of pressure, the initial DO at the effluent is significantly increased above the DO at the CDI inlet. However, the concentration of DO at the CDI cell's effluent gradually reduces and stabilizes to a similar level as that which is obtained from the experiment without the application of pressure, and on a time scale as indicated in Figure 4.2 since no inert purge gas was applied to the liquid reservoir.
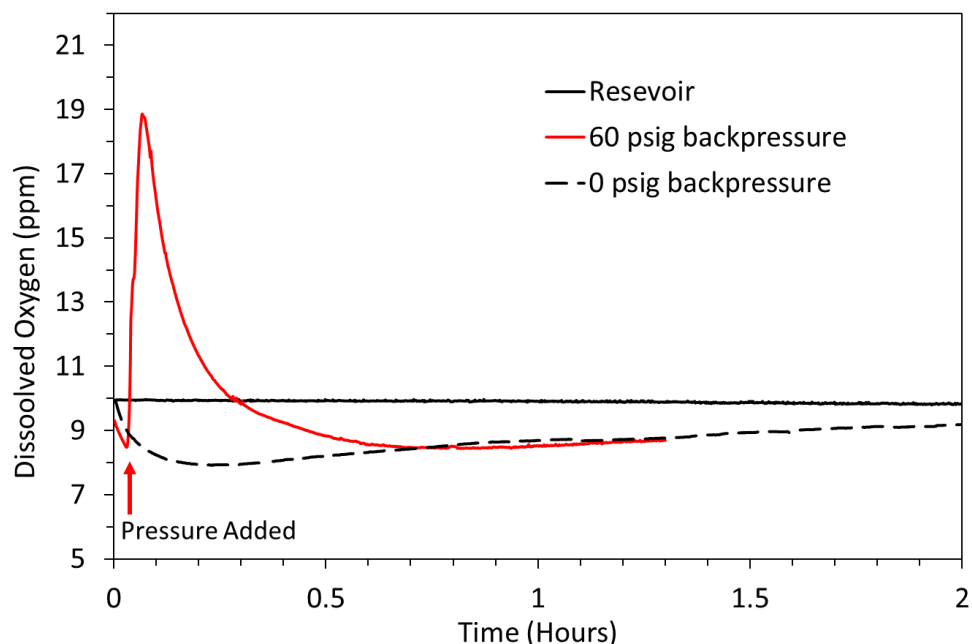
Figure 4.2: Dissolved oxygen profiles for flow-through CDI cells exposed to 0 psig and 60 psig of added backpressure compared to the reservoir baseline DO level. Time zero refers to the introduction of the cell to 16 mL/min saline solution flow rate. Note that added backpressure refers to the pressure regulator's addition to the total pressure on the system.

The application of system pressure to the flow-through cell causes oxygen, trapped in the electrodes' pores, to dissolve in accordance with Henry's law and exit the cell entrained in the flow of solution. The amount of DO removed from the cell during initial pressurization is the area between the pressurized effluent and the non-pressurized effluent in Figure 4.2, amounting to between 0.2 mg and 0.4 mg of oxygen per gram of electrode. This corresponds to 30% -40% of the total oxygen in the pore space of dry Kynol ACC (e.g. the dead-end pore defined in Figure 2.13) based upon the manufacturer's specified pore volume; however, no remarkable SAC increase was seen under pressurized operation. This is because the dead-end pores are likely not playing a role in salt adsorption, due to lack of flow, and it is likely that pH swings associated with the application of a flow-through cell structure also impede capacitive storage. Ion adsorption and oxygen adsorption/reaction

are independent processes competing for the active adsorption sites on the surface of the electrodes. The carbon's natural affinity for oxygen in its pristine condition causes significant amounts to be available for faradaic reactions in the initial charging cycles leading to high rates of degradation.

4.2. Flow-Through Results

4.2.1. Capacity Results

Although the benefits of operating at increased pressures do not exemplify an ion adsorption capacity increase, after a few charge cycles the cells operated at an elevated pressure began to outperform the non-pressurized cells, maintaining a higher SAC through more cycles. Figure 4.3A displays this degradation trend as a percent decrease in capacity compared to the first cycle capacity when cycled between a charging voltage of 0.9 V and a discharging voltage of 0 V, achieved through a physical short circuit between the electrodes.
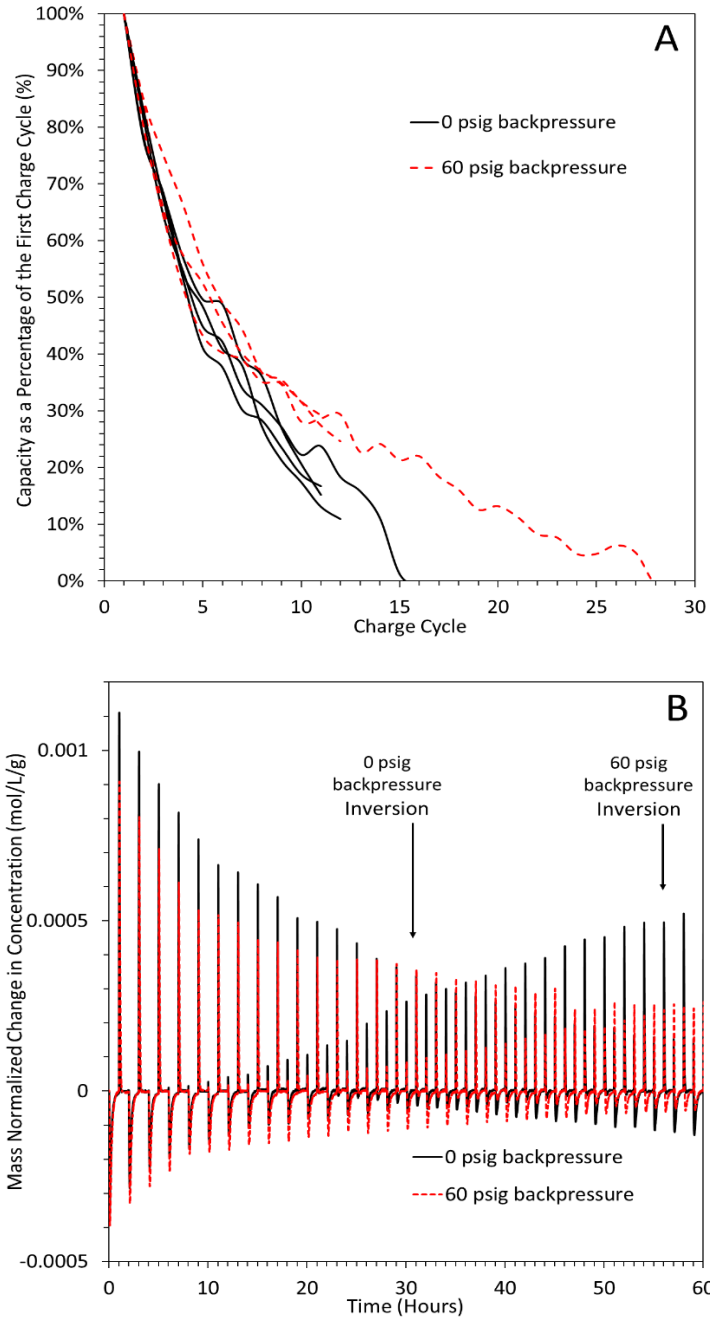
Figure 4.3: Comparison between the cells operated at 0 psig and 60 psig backpressure. (A) shows the change in SAC as a percentage of the nominal capacity of 5 mg/g, demonstrating a difference in the rate of degradation, and (B) shows the concentration profiles marking points of inversion where the net SAC is zero during the applied potential portion of the cycle.

Figure 4.3B displays this degradation trend in terms of inversion spikes in the effluent concentration profile that signify co-ion desorption and begin to occur at the start of each charging event. Concentration data in mol/L is converted from conductivity data using the probe specific conversion (1 μS/cm = 8.87×10^{-6} mol/L). Thus, from the concentration profile, another metric for the rate of cell degradation is the growth rate of these inversion spikes (16, 33, 41, 46). Once co-ion desorption is equal to counter-ion adsorption under a charging event, the cell has reached its maximum utility under conventional CDI operation at the applied potential. Figure 4.3B further shows that the cell operated with no backpressure reached the inversion point in the 30th hour of operation where the cell operated with 60 psig backpressure did not reach the inversion point until the 56th hour of operation. This time difference between the appearances of the inversion point for each of the pressure conditions signifies an 86.7% increase in cell life. Additionally, the non-pressurized cell, containing 4 g of carbon, adsorbed 24.2 mg/g in its 30 hour life and the pressurized cell, containing 4.4 g of carbon, adsorbed 41.7 mg/g in its 56 hour life, which is a 72.8% increase in lifetime salt adsorption.

4.2.2. Current & DO Results

Considering the faradaic reactions mentioned previously, we can neglect the occurrence of oxygen evolution, the reverse of Equation 2.10, in our cells because our charging voltage is only 0.9 V, which is below the 1.23 V typically required for the oxygen evolution reaction. This leaves oxygen reduction, Equation 2.10, and carbon oxidation, Equation 2.11, which have higher driving forces compared to hydrogen evolution, Equation 2.12,

allowing us to neglect it as well. During the applied potential portion of the cycle there are two independent processes competing for the current passed between the electrodes, ion adsorption and the faradaic reactions. Once the electrodes reach ion adsorption capacity, the only remaining passage of current is due to the irreversible faradaic redox pair occurring in equilibrium at the cathode and anode. The cathodic reaction brings about another performance metric for faradaic reactions, the consumption of dissolved oxygen. Pairing the leakage current and the consumption of dissolved oxygen gives a strong indicator of the occurrence of faradaic reactions where higher leakage current and more oxygen consumption, when seen together, indicate more faradaic reactions. Figure 4.4A and 4.4B show that the CDI cells operated with 60 psig backpressure have a leakage current averaging 5.6 mA/g and reduce the effluent DO to around 0.5 ppm in the 10th-15th cycles. In the same range of cycles, the cells operated at ambient pressure had a leakage current of 7-8 mA, and increasing, while reducing the effluent DO to around 0.35 ppm. It is believed that the electroactive oxygen is a combination of DO in the electrodes' pore space and DO brought by the feed-stream via transportation from the bulk to the pores (43, 70). Thus, the decreased consumption of DO by the pressurized cell could be explained by the reduced driving force to diffuse DO trapped in the electrodes' pore space, similar to the effects of purging the reservoir with nitrogen. Furthermore, in comparing the Henry's law constants for oxygen and nitrogen, 769 and 1590 (L*Atm/mol) (69) respectively, a given increase in pressure will result in higher dissolution of oxygen than nitrogen, effectively increasing the inactivity of any gases not removed from the cell.
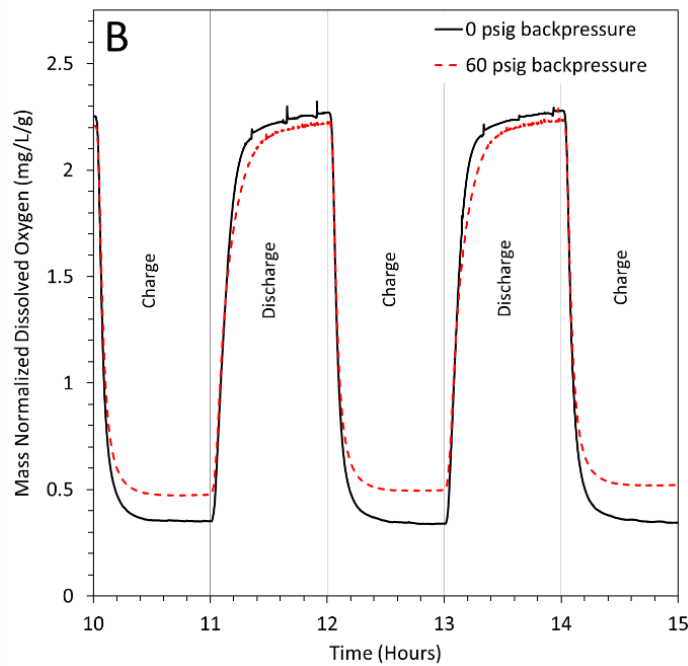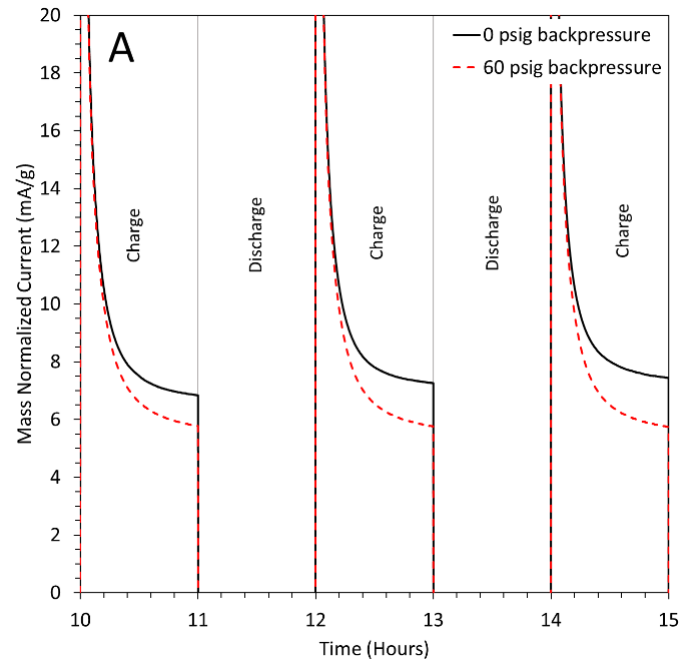
Figure 4.4: Cells operated at 0 psig and 60 psig backpressure with charge/discharge voltages of 0.9/0.0 V. (A) Mass normalized current profile decreased leakage current at 60 psig backpressure. (B) Mass normalized DO profiles showing decreased oxygen consumption during charging at 60 psig backpressure.

4.2.3. Post Examination of Electrodes

After deaerating 100 mL of 5 mM NaCl solution through nitrogen purging, cyclic voltammetry was performed. A scanning range between -0.6 and 0.8 V and a scan rate of 1 mV/s were used to determine the E_{PZC} locations of pristine Kynol, Figure 4.5A, and anodes extracted from cells operated at 0 and 60 psig backpressure for 65 hours, Figure 4.5B. Comparing the E_{PZC} locations of pristine Kynol to the anodes from cells cycled for 65 hours shows a significant E_{PZC} shift due to the prolonged operation, as is expected and described previously in Figure 2.12. Initial E_{PZC} data between pressure conditions, shown in Figure 4.5B, appears to further validate the degradation rate difference between the two; however, further testing is required for a more pronounced difference in the E_{PZC} locations of pressurized and non-pressurized cells.
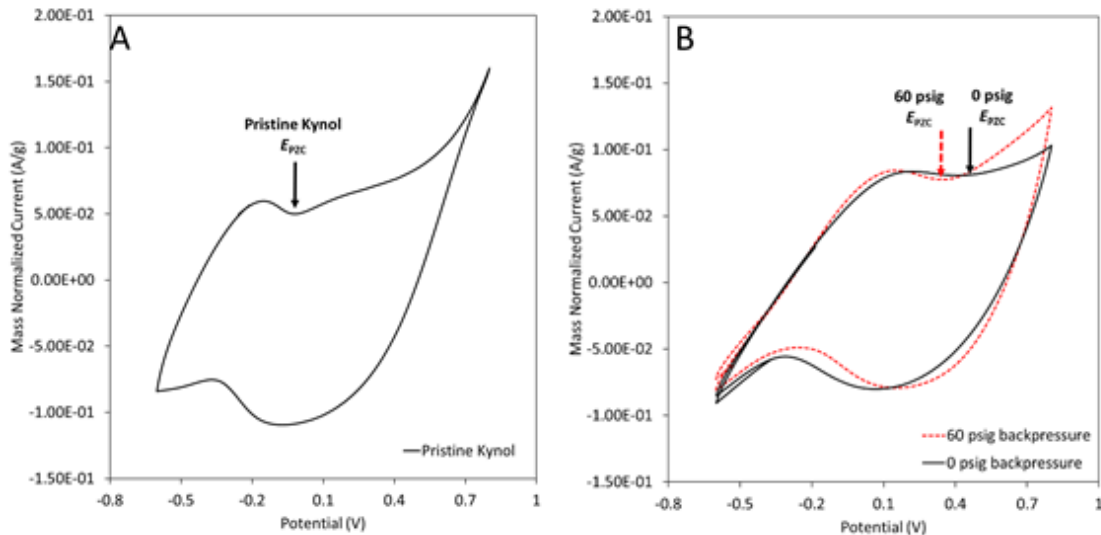
Figure 4.5: Cyclic voltammetry in 5 mM NaCl solution, deaerated through a nitrogen purge, demonstrating the location of the E_{PZC} for (A) pristine Kynol ACC, and (B) 0 psig vs. 60 psig anodes after 65 hours of CDI operation demonstrating that the anode cycled without pressure has oxidized further.

4.3. Energy and Cost Assessment

4.3.1. CDI Pressurized vs Non-pressurized

For the purpose of this experimentation, the initial capital costs for building the cell (minus the electrodes) are ignored because the addition of 60 psig backpressure does not require the cell to be altered; however, for the application of higher operational backpressures, capital costs could increase. In assessing the recurring costs associated with continuous CDI operation, electricity costs due to the cell charging voltage and pump operation must be considered as well as the cost of replacing the electrodes at the end of their useful life.

Assuming an average electricity price in the United States to be \$0.12/kWhr, the instantaneous power consumed during the charging phase was calculated using Equation 4.2, which assumes no energy recovery from the discharge phase of the cell.

$$E_{charge} = \int_{0}^{3600} \frac{I}{m_{carbon}} \, dt * V_{cell} \quad (Joules/g) \qquad [4.2]$$

Where, I is the current passed between electrodes during the application of voltage, $V_{cell} = 0.9$ V, and m_{carbon} is the mass of carbon in grams, allowing the charging cost to be scalable by mass of electrode. In assessing the cost for an hour of operation, E_{charge} is energy consumed during the hour charging cycle and dividing by 3600 sec. gives the energy consumed during the hour in terms of watt*hours. The cost associated with charging is calculated using Equation 4.3, using the average energy consumed per hour of charging to account for variations as the cell degrades.

$$C_{charge} = \frac{E_{charge,avg}}{1000} * m_{carbon} * \$0.12 * \frac{t_{op}}{2} \qquad [4.3]$$

In Equation 4.3, C_{charge} is the cost incurred due to charging the cell, $E_{charge,avg}$ is the average energy consumed during an hour of charging (averaged over every cycle of the cell's life), and t_{op} is the operational time, in hours. Note that the operational time in Equation 4.3 is halved because the charging phase is only half of each cycle; therefore, the cell only has applied potential for half of the operational time.

The other electricity-based operational cost is incurred through powering the pump. Power consumed by the pump in calculated in Equation 4.4.

$$P_{pump} = \frac{\dot{V}\rho g h}{\eta} \ (Watts) \qquad [4.4]$$

Where, $\dot{V}$ is the volumetric flow rate (m³/sec.), ρ is the density of the fluid taken to be water at 1000 kg/m³, g is acceleration due to gravity (9.81 m/s²), h is the hydrostatic head-pressure in meters of water, and η is the efficiency of the pump, assumed to be 90% for a piston pump. The cost associated with powering the pump is calculated similarly to the cost for applying voltage across the cell. E_{pump} (Watt*hours) is merely P_{pump} * 1 hour, providing C_{pump} in Equation 4.5.

$$C_{pump} = \frac{E_{pump}}{1000} * \$0.12 * t_{op} \qquad [4.5]$$

Note that t_{op} is not halved in the pumping cost calculation because the pump in still working during the discharging portion of operation.

The final recurring cost for CDI operation is the replacement of the electrodes. This cost will change with the pressurization condition due to the cell-life changes brought about by pressurized operation. Carbon replacement costs are calculated using Equation 4.6, show below.

$$C_{carbon} = x_{carbon} * m_{carbon} * \frac{t_{op}}{t_{life}}$$ [4.6]

In Equation 4.6, x_{carbon} is the price of carbon per gram, m_{carbon} is the mass of electrode material in grams, and t_{life} is the life of the cell in hours. Therefore, the ratio of t_{op} to t_{life} is the number of times that the cell must be replaced during the specified operational time.

In comparing the cost of normal, non-pressurized, operation to pressurized operation, the carbon and flow rate were slightly increased from the laboratory scale at which experimentation was conducted in order to make the numbers more easily comparable. The charging cost and carbon replacement cost appropriately scaled as the mass of electrodes increased, and the pumping cost scale by the hydrostatic pressure increase. Hydrostatic pressure is a combination of the pressure drop due to flow resistance across the cell and the additionally applied backpressure. When the mass of carbon and flow rate both increase, the pressure drop due to flow resistance will also increase affecting all cells the same regardless of the amount of additional backpressure applied. The operational parameters included in the cost comparison can be found is Table 4.2.

Table 4.2: CDI operational parameters.

Operational Parameter	Units	0 psig Backpressure	60 psig Backpressure
Avg. Current / Charge Cycle	(Amps)	8.954	8.385
Applied Voltage	(Volts)	0.9	0.9
Flow Rate	(L/min)	4	4
Pressure drop	(psig)	10	10
Backpressure	(psig)	0	60
Electrode Mass/Cell	(grams)	1000	1000
Continuous Operation Time	(hours)	720 (1 month)	720 (1 month)
Cell Life	(hours)	36	60
Price of Kynol	($/gram)	$1.08	$1.08
Price of General Carbon	($/gram)	$0.004	$0.004

Using the operational parameters outlined above and Equations 4.2 – 4.6, a breakdown of the cost difference between pressurized and non-pressurized cells was calculated and can be seen in Table 4.3, below. The vast difference in cost between Kynol and general carbon is due to Kynol being an extremely high grade carbon with tight quality control. For this reason, Kynol was used in experimentation to minimize the effects that carbon variation could have on test results when each cell has only 4 g of carbon. Large scale production of Kynol is currently not cost competitive; therefor, this cost comparison also includes a scenario utilizing a general carbon material that is more cost competitive for large scale industrial use. This substitution could be made because quality control would not be as crucial when the total mass of carbon increases to the kilogram scale or even larger.

Table 4.3: Cost summary of CDI operation for 1 month with 1 kg of carbon/per cell.

Backpressure	C_{pump}	C_{charge}	$C_{carbon,Kynol}$	$C_{carbon,gen}$	$C_{Total,kynol}$	$C_{Total,gen.}$
0 psig:	$0.44	$0.35	$21,600.00	$80.00	**$21,600.79**	**$80.79**
60 psig:	$3.09	$0.33	$12,960.00	$48.00	**$12,963.42**	**$51.42**

As can be seen from Table 4.3, there is an increased cost for pumping the solution to a higher pressure. This increased cost is however negated by the increased life of the pressurized electrodes, meaning that they will not need replacing as often as the non-pressurized electrodes. The cost savings seen from the increased life of the electrodes far outweighs the cost incurred by the extra energy going to the pump. In summary, even under the assumption of carbon being much cheaper than the Kynol used in this experimentation, the cost of more frequently replacing the electrodes in a non-pressurized cell is much higher than the cost of pressurizing the cell by an additional 60 psig.

4.3.2. Pressurized CDI vs RO

Extrapolating further on the cost of CDI operation we can compare to reverse osmosis, one of the most prevalent desalination technologies for industrial application. The benchmark used for comparison is laid out by Karagiannis et al. (71) who cited RO for brackish water to cost between \$0.78 and \$1.33 per m^3 of water desalinated for a plant producing between 20 m^3/day and 1200 m^3/day of fresh water (72-75). Assuming that the inlet concentration is 4000ppm and the recovered effluent is down to 1000ppm, Equations 4.2 – 4.6 can again be used to produce Figure 4.6.
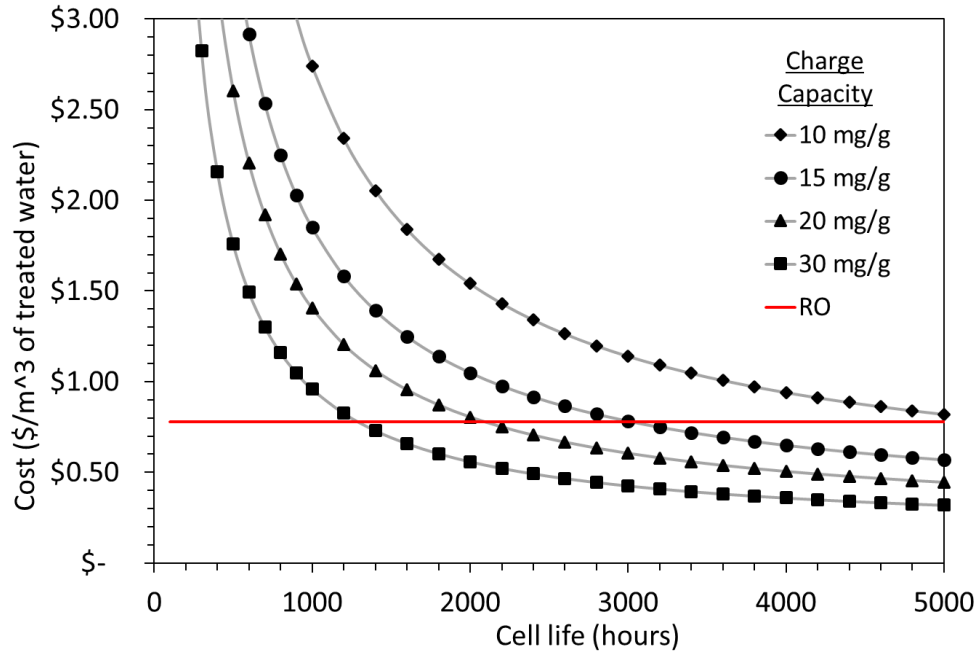
Figure 4.6: Cost comparison between pressurized CDI and RO on the cost to sustain production of 1200 m³/day of fresh water from a 4000 ppm brackish stream.

Figure 4.6 shows the break-even points for pressurized CDI compared to RO at a few charge capacities. As the average SAC for the cell increases, the mass of carbon required to meet the desalination mark decreases and with it the cost to sustain operation. Although the capacity of the cells used in this experimentation were small, SAC values of around 30 mg/g are possible from some of today's more advanced capacitive deionization systems (54, 60, 76). Figure 4.6 also shows that as the cell life increases, the costs to sustain operation decreases because the electrodes do not need replaced as frequently, as previously discussed. Considering that the productive life of today's CDI technology is well below 1000 hours, Figure 4.6 also explains why increases in cell life have such a drastic effect on operating costs, which is depicted by the extreme slopes of the curves in this region of the graph. Even a slight increase in cell life will have a large impact on operating costs, which will only grow with sustained operation.

5. Conclusion

Experimentation began with a comparison between flow-through and flow-by CDI cell structures operated with pristine Kynol ACC electrodes and with no additional backpressure. Through an increased SAR as demonstrated by a Ragone (Kim-Yoon) plot, flow-through cells typically outperform flow-by cells in the initial charging cycle. Although cell degradation tends to be worse for flow-through cells than flow-by, the flow-through cell structure was chosen as the model for further testing. This selection was due to the importance of the salt adsorption rate for scaled up, industrial, continuous operation.

In an attempt to manage air bubbles that could be trapped in the pore space of the nano-porous carbon electrodes, backpressure was introduced to the system. Theorizing that, through the application of Henry's law, the addition of backpressure would cause trapped oxygen to dissolve and exit the cell through entrainment in the flow, and two experimental pressure conditions were tested. Both pressurization cases had an excess of air bubbled in the reservoir during CDI operation maintaining a solution saturated with dissolved oxygen at atmospheric pressure at the entrance to the system. Saturating the reservoir eliminated any compounding effects from solution oxygen content returning to the reservoir. This effectively isolated the consequences of the additional backpressure or lack thereof with respect to the DO profiles in Section 4.1. This initial data showed that the addition of backpressure allowed the removal of approximately 0.3 mg of oxygen per gram electrode, which corresponds to between 30% and 40% of the oxygen present in the dry Kynol carbon, based on the manufacturer's specified pore volume. In other words, pressurization helps

evacuate gaseous oxygen that remains in the cell after the initial wetting and introduction to flowing solution.

The effect that system pressure had on CDI performance lacked a notable SAC increase; however, the cells operated with a system pressure of 60 psig held their SAC values longer than the cells operated at 0 psig. This increased cell life, to the sum of 26 hours, marks an 86.7% increase in cycle number and led to a 72.8% increase in productivity, or lifetime salt adsorption. These results are further corroborated by the faster appearance and increased growth rate of the inversion spike at the beginning of the charging events. This inversion spike signifies the amount of co-ion desorption in the charging event and marks the progression of the cell from traditional CDI, applied potential-driven adsorption, to inverted CDI, chemical surface-charge driven adsorption. This switch marks the end-of-life for conventional CDI operation at the applied potential.

Additionally, in accumulation with the capacity data, under pressurized operation, the combination of lower leakage current and less dissolved oxygen consumption during charging lends strong support to the conclusion of decreased faradaic reactions. Initial data from post examination of the electrodes shows that CDI operation under backpressure led to a slightly smaller positive shift in the anodes' E_{PZC} values. This also supports the aforementioned decreased rate of degradation seen in the salt adsorption capacity data, and operating the cells longer should provide a more significant difference in E_{PZC} location for the two pressure conditions.

Finally, in the cost assessment, it can be seen that, although CDI operation under pressure does accrue more pumping costs, the 86.7% increase in productive cycles of operation makes operating under pressure cheaper when continuous operation is assumed. The relatively short life times for CDI cells in comparison to other desalination methods make the cost of replacing the electrodes much more impactful than the pumping costs. As seen in the direct comparison between CDI and RO, discussed in Section 4.3.2, the productive life and the capacity of CDI both need further improvement in order to meet the benchmark set by RO systems. Although the abilities of the CDI cells used in this experimentation are far from competitive with RO, the concept of using additional backpressure to combat the side effects of dissolved oxygen can be applied present and future superior CDI technologies, allowing them to further improve their stability and productive life times.

REFERENCES

1. J. F. Kenny, N. L. Barber, S. S. Hutson, K. S. Linsey, J. K. Lovelace and M. A. Maupin, Estimated use of water in the United States in 2005, in *Circular*, p. 60, Reston, VA (2009).
2. D. S. Lumia, K. S. Linsey and N. L. Barber, *Estimated use of water in the United States in 2000*, US Department of the Interior, US Geological Survey (2005).
3. M. A. Maupin, J. F. Kenny, S. S. Hutson, J. K. Lovelace, N. L. Barber and K. S. Linsey, Estimated use of water in the United States in 2010, in *Circular*, p. 64, Reston, VA (2014).
4. M. A. Anderson, A. L. Cudero and J. Palma, *Electrochimica Acta*, **55**, 3845 (2010).
5. Y. Oren, *Desalination*, **228**, 10 (2008).
6. J. Landon, X. Gao, B. Kulengowski, J. K. Neathery and K. Liu, *Journal of the Electrochemical Society*, **159**, A1861 (2012).
7. F. He, P. M. Biesheuvel, M. Z. Bazant and T. A. Hatton, *Water research*, **132**, 282 (2018).
8. P. Srimuk, M. Zeiger, N. Jäckel, A. Tolosa, B. Krüner, S. Fleischmann, I. Grobelsek, M. Aslan, B. Shvartsev, M. E. Suss and V. Presser, *Electrochimica Acta*, **224**, 314 (2017).
9. N. Holubowitch, A. Omosebi, X. Gao, J. Landon and K. Liu, *ChemElectroChem*, **4**, 2404 (2017).
10. C. Zhang, D. He, J. Ma, W. Tang and T. D. Waite, *Water research*, **128**, 314 (2017).
11. S. Porada, R. Zhao, A. van der Wal, V. Presser and P. M. Biesheuvel, *Progress in Materials Science*, **58**, 1388 (2013).
12. M. E. Suss, S. Porada, X. Sun, P. M. Biesheuvel, J. Yoon and V. Presser, *Energy & Environmental Science*, **8**, 2296 (2015).
13. M. Z. Bazant, K. Thornton and A. Ajdari, *Physical Review E*, **70**, 021506 (2004).
14. Y. Bouhadana, E. Avraham, A. Soffer and D. Aurbach, *AIChE Journal*, **56**, 779 (2010).
15. E. Avraham, M. Noked, Y. Bouhadana, A. Soffer and D. Aurbach, *Electrochimica Acta*, **56**, 441 (2010).
16. I. Cohen, E. Avraham, Y. Bouhadana, A. Soffer and D. Aurbach, *Electrochimica Acta*, **106**, 91 (2013).
17. S. Evans and W. S. Hamilton, *Journal of The Electrochemical Society*, **113**, 1314 (1966).
18. S. Evans, M. A. Accomazzo and J. E. Accomazzo, *Journal of The Electrochemical Society*, **116**, 307 (1969).
19. W. Tang, D. He, C. Zhang, P. Kovalsky and T. D. Waite, *Water research*, **120**, 229 (2017).
20. D. He, C. E. Wong, W. Tang, P. Kovalsky and T. D. Waite, *Environmental Science & Technology Letters*, **3**, 222 (2016).
21. S. Shanbhag, J. F. Whitacre and M. S. Mauter, *Journal of The Electrochemical Society*, **163**, E363 (2016).
22. A. M. Johnson and W. VENOLIA, (1970).
23. A. M. Johnson and J. Newman, *Journal of The Electrochemical Society*, **118**, 510 (1971).
24. Y. Oren and A. Soffer, *Journal of The Electrochemical Society*, **125**, 869 (1978).
25. R. H. Wilhelm, A. W. Rice and A. R. Bendelius, *Industrial & Engineering Chemistry Fundamentals*, **5**, 141 (1966).
26. R. W. Pekala, J. C. Farmer, C. T. Alviso, T. D. Tran, S. T. Mayer, J. M. Miller and B. Dunn, *Journal of Non-Crystalline Solids*, **225**, 74 (1998).
27. M. E. Suss, T. F. Baumann, W. L. Bourcier, C. M. Spadaccini, K. A. Rose, J. G. Santiago and M. Stadermann, *Energy & Environmental Science*, **5**, 9511 (2012).
28. C.-M. Yang, W.-H. Choi, B.-K. Na, B. W. Cho and W. I. Cho, *Desalination*, **174**, 125 (2005).
29. C. J. Gabelich, T. D. Tran and I. H. M. Suffet, *Environmental science & technology*, **36**, 3010 (2002).
30. P. Xu, J. E. Drewes, D. Heil and G. Wang, *Water research*, **42**, 2605 (2008).

31. R. L. Zornitta, F. J. García-Mateos, J. J. Lado, J. Rodríguez-Mirasol, T. Cordero, P. Hammer and L. A. M. Ruotolo, *Carbon*, **123**, 318 (2017).
32. J. J. Wouters, J. J. Lado, M. I. Tejedor-Tejedor, R. Perez-Roa and M. A. Anderson, *Electrochimica Acta*, **112**, 763 (2013).
33. X. Gao, A. Omosebi, J. Landon and K. Liu, *Journal of The Electrochemical Society*, **161**, E159 (2014).
34. T. Kim and J. Yoon, *RSC Advances*, **5**, 1456 (2015).
35. S. Porada, L. Borchardt, M. Oschatz, M. Bryjak, J. S. Atchison, K. J. Keesman, S. Kaskel, P. M. Biesheuvel and V. Presser, *Energy & Environmental Science*, **6**, 3700 (2013).
36. E. Avraham, Y. Bouhadana, A. Soffer and D. Aurbach, *Journal of The Electrochemical Society*, **156**, P95 (2009).
37. P. Srimuk, F. Kaasik, B. Kruner, A. Tolosa, S. Fleischmann, N. Jackel, M. C. Tekeli, M. Aslan, M. E. Suss and V. Presser, *Journal of Materials Chemistry A*, **4**, 18265 (2016).
38. Y. Qu, T. F. Baumann, J. G. Santiago and M. Stadermann, *Environmental Science & Technology*, **49**, 9699 (2015).
39. J. Landon, X. Gao, A. Omosebi and K. Liu, in *Submicron Porous Materials*, P. Bettotti Editor, p. 1, Springer International Publishing, Cham (2017).
40. X. Gao, A. Omosebi, N. Holubowitch, J. Landon and K. Liu, *Electrochimica Acta*, **233**, 249 (2017).
41. X. Gao, A. Omosebi, J. Landon and K. Liu, *Energy Environ. Sci.*, **8**, 897 (2015).
42. A. Omosebi, X. Gao, J. Landon and K. Liu, *ACS Applied Materials & Interfaces*, **6**, 12640 (2014).
43. B. Shapira, E. Avraham and D. Aurbach, *Electrochimica Acta*, **220**, 285 (2016).
44. M. Noked, E. Avraham, A. Soffer and D. Aurbach, *The Journal of Physical Chemistry C*, **113**, 21319 (2009).
45. Z.-H. Huang, M. Wang, L. Wang and F. Kang, *Langmuir*, **28**, 5079 (2012).
46. I. Cohen, E. Avraham, Y. Bouhadana, A. Soffer and D. Aurbach, *Electrochimica Acta*, **153**, 106 (2015).
47. E. Avraham, M. Noked, Y. Bouhadana, A. Soffer and D. Aurbach, *Journal of the Electrochemical Society*, **156**, P157 (2009).
48. E. Avraham, M. Noked, I. Cohen, A. Soffer and D. Aurbach, *Journal of the Electrochemical Society*, **158**, P168 (2011).
49. E. Avraham, M. Noked, A. Soffer and D. Aurbach, *Electrochimica Acta*, **56**, 6312 (2011).
50. X. Gao, A. Omosebi, J. Landon and K. Liu, *The Journal of Physical Chemistry C*, **122**, 1158 (2018).
51. X. Gao, S. Porada, A. Omosebi, K. L. Liu, P. M. Biesheuvel and J. Landon, *Water research*, **92**, 275 (2016).
52. A. Omosebi, X. Gao, N. Holubowitch, Z. Li, J. Landon and K. Liu, *Journal of The Electrochemical Society*, **164**, E242 (2017).
53. M.-W. Ryoo, J.-H. Kim and G. Seo, *Journal of Colloid and Interface Science*, **264**, 414 (2003).
54. S. Kim, J. Lee, C. Kim and J. Yoon, *Electrochimica Acta*, **203**, 265 (2016).
55. C.-H. Hou, C. Liang, S. Yiacoumi, S. Dai and C. Tsouris, *Journal of Colloid and Interface Science*, **302**, 54 (2006).
56. H. Li, L. Pan, T. Lu, Y. Zhan, C. Nie and Z. Sun, *Journal of Electroanalytical Chemistry*, **653**, 40 (2011).
57. C. Nie, L. Pan, H. Li, T. Chen, T. Lu and Z. Sun, *Journal of Electroanalytical Chemistry*, **666**, 85 (2012).
58. C. Nie, L. Pan, Y. Liu, H. Li, T. Chen, T. Lu and Z. Sun, *Electrochimica Acta*, **66**, 106 (2012).

59. L. Pan, X. Wang, Y. Gao, Y. Zhang, Y. Chen and Z. Sun, *Desalination*, **244**, 139 (2009).
60. Y. Huang, F. Chen, L. Guo and H. Y. Yang, *Journal of Materials Chemistry A*, **5**, 18157 (2017).
61. P. Srimuk, L. Ries, M. Zeiger, S. Fleischmann, N. Jackel, A. Tolosa, B. Kruner, M. Aslan and V. Presser, *RSC Advances*, **6**, 106081 (2016).
62. Z. Peng, D. Zhang, L. Shi and T. Yan, *Journal of Materials chemistry*, **22**, 6603 (2012).
63. D. Zhang, T. Yan, L. Shi, Z. Peng, X. Wen and J. Zhang, *Journal of Materials Chemistry*, **22**, 14696 (2012).
64. M. Haro, G. Rasines, C. Macias and C. O. Ania, *Carbon*, **49**, 3723 (2011).
65. X. Shang, R. D. Cusick and K. C. Smith, *Journal of The Electrochemical Society*, **164**, E536 (2017).
66. J.-H. Lee, W.-S. Bae and J.-H. Choi, *Desalination*, **258**, 159 (2010).
67. L. Han, K. G. Karthikeyan, M. A. Anderson and K. B. Gregory, *Journal of Colloid and Interface Science*, **430**, 93 (2014).
68. J. L. Sotelo, F. J. Beltrán, F. J. Benitez and J. Beltrán-Heredia, *Water research*, **23**, 1239 (1989).
69. M. M. Benjamin and D. F. Lawler, *Water Quality Engineering: Physical/Chemical Treatment Processes*, John Wiley & Sons, Inc., Hoboken, New Jersey (2013).
70. A. M. Oickle and H. A. Andreas, *The Journal of Physical Chemistry C*, **115**, 4283 (2011).
71. I. C. Karagiannis and P. G. Soldatos, *Desalination*, **223**, 448 (2008).
72. Y. Al-Wazzan, M. Safar, S. Ebrahim, N. Burney and A. Mesri, *Desalination*, **143**, 21 (2002).
73. I. S. Jaber and M. R. Ahmed, *Desalination*, **165**, 209 (2004).
74. I. C. Karagiannis and P. G. Soldatos, *Desalination*, **203**, 56 (2007).
75. D. Sambrailo, J. Ivić and A. Krstulović, *Desalination*, **179**, 339 (2005).
76. F. Chen, Y. Huang, L. Guo, L. Sun, Y. Wang and H. Y. Yang, *Energy & Environmental Science*, **10**, 2081 (2017).

VITA

Name:

Landon Scott Caudill

Place of Birth:

Nicholasville, KY, USA

Education:

University of Kentucky

Bachelor of Science in Mechanical Engineering May 2016

Positions Held:

Undergraduate Engineering Intern

Center for Applied Energy Research, University of Kentucky

May 2014-August 2016

Graduate Research Assistant

Center for Applied Energy Research, University of Kentucky

August 2016- May 2018

Publications:

Landon Caudill, A. Omosebi, X. Gao, James Landon, and K. Liu, (2018). In-Situ De-Aeration Towards Performance Stability of Capacitive Deionization Cells. Meeting Abstracts, MA2018-01(20), 1289-1289.

Landon Caudill, A. Omosebi, X. Gao, James Landon, and K. Liu, (2018). In-Situ De-Aeration Towards Performance Stability of Capacitive Deionization Cells, *accepted for publication in Electrochemical Society (ECS) Transactions.*

Conferences and Presentations:

Landon Caudill, A. Omosebi, X. Gao, James Landon, and K. Liu, (2018, May). In-Situ De-Aeration Towards Performance Stability of Capacitive Deionization Cells Oral Presentation at 233 Electrochemical Society, Seattle, WA.